CHALMERS
UNIVERSITY OF TECHNOLOGY

A Novel Tropospheric Error Formula for Ground-based GNSS Interferometric Reflectometry

Citation for the original published paper (version of record):
Feng, P., Haas, R., Elgered, G. (2023). A Novel Tropospheric Error Formula for Ground-based GNSS Interferometric Reflectometry. IEEE Transactions on Geoscience and Remote Sensing, 61: 1-18. http://dx.doi.org/10.1109/TGRS.2023.3332422

(article starts on next page)

A Novel Tropospheric Error Formula for Ground-Based GNSS Interferometric Reflectometry

Peng Feng, *Member, IEEE*, Rüdiger Haas, and Gunnar Elgered

***Abstract*— We deduce a novel interferometric tropospheric error (NITE) formula for ground-based global navigation satellite system interferometric reflectometry (GNSS-IR). This formula contains two parts: a geometric displacement error that accounts for the reflection point change due to the atmosphere and Earth's curvature, and a path delay derived following the definition of the mapping function (with the small curve path effect included). We validate the NITE formula together with two previously used approaches: the bending angle correction and the mapping function path delay (MPF delay) using raytracing and radiosonde data. The raytracing results show that the NITE formula is more accurate than the previous approaches. Numerically, the geometric displacement error is <5% of the path delay error for a GNSS antenna located 20 m above sea level. We further evaluate six tropospheric correction strategies for GNSS-IR sea-level monitoring through two sets of experiments. With an elevation angle range test, we show that applying no tropospheric correction and applying the bending angle correction plus the MPF delay both introduce large elevation-dependent biases. Analyzing the time series of differences between GNSS-IR and tide gauges sea level, we show that the bending angle correction with the widely used Bennett equation introduces long-term (4 h to several months) trends in the sea-level retrievals. We identify one station where the NITE formula produces better long-term (τ > 4 h) sea-level retrievals. Finally, we show that at low elevation angles, the bending angle correction can be reformulated as an MPF delay.**

***Index Terms*— Earth's curvature, global navigation satellite system interferometric reflectometry (GNSS-IR), raytracing, sea-level monitoring, tropospheric error.**

I. Introduction

THE application of global navigation satellite system (GNSS) has been successfully extended from positioning, navigation, and timing (PNT) [1], [2] to environmental remote sensing. GNSS is today used, e.g., in meteorology [3], to study the atmosphere [4], soil moisture [5], [6], and so on. GNSS reflectometry is one of these new applications, which uses the reflected GNSS signal to study the surrounding environment. For positioning, the reflected signals from nearby objects are regarded as an error source, referred to as the multipath error [7]. In GNSS reflectometry, by investigating the reflected signal and its interaction with the direct signal, we can measure snow depth, sea level, and so on.

Manuscript received 17 March 2023; revised 12 July 2023 and 4 October 2023; accepted 5 November 2023. Date of publication 13 November 2023; date of current version 27 November 2023. This work was supported by a grant from the Hasselblad Foundation. *(Corresponding author: Peng Feng.)*

The authors are with the Department of Space, Earth and Environment, Chalmers University of Technology, Onsala Space Observatory, SE-439 92 Onsala, Sweden (e-mail: peng.feng@chalmers.se).

Digital Object Identifier 10.1109/TGRS.2023.3332422

A typical setup for monitoring sea level using GNSS interferometric reflectometry (GNSS-IR) is to install a GNSS antenna near the coastline, where it can receive the combination of direct satellite signals and signals reflected off the sea surface. The reflected signal travels a longer distance to reach the antenna than the direct one. As a satellite ascends or descends, the phase lag between the reflected and the direct signal changes, resulting in a periodic variation in the power of the received signal at the antenna. The power is recorded by GNSS receivers as a signal-to-noise ratio (SNR); hence, this method is also known as the SNR-based GNSS-IR. By determining the frequency of this varying SNR as a function of elevation angle, we can derive the reflector height H_r from the GNSS antenna to the sea surface. With a simplified (vacuum and planar reflection) geometry, the relationship between reflector height H_r and the reflected-versus-direct interferometric radio length τ_i can be written as [8], [9]

$$\tau_i = 2H_r \sin e_T \tag{1}$$

where e_T is the true elevation angle [10] of the satellite at the GNSS antenna.

GNSS-IR gives the height difference between the GNSS antenna and the sea surface. In combination with the inherent positioning ability of GNSS, GNSS-IR can provide sea-level measurements with precision close to traditional tide gauges [11] in a well-determined global terrestrial reference frame. This is called absolute sea-level monitoring. The temporal resolution of GNSS-IR sea-level results is also improving, thanks to the development of multi-GNSS [12], [13]. However, systematic biases were found between GNSS-IR and traditional tide gauges [14], [15], which impairs the advantage of the absolute sea-level monitoring ability of GNSS-IR.

To enhance interferometric patterns, GNSS-IR tends to use low elevation angle observations (down to 2°). However, the tropospheric error becomes more pronounced at lower elevation angles. Several studies have been dedicated to tropospheric errors in GNSS-IR. Santamaría-Gómez and Watson [16] examined the elevation-(angle)-dependent error on GNSS-IR and proposed the bending angle correction with an equation by Bennett [17]. The Bennett equation is now widely adopted in GNSS-IR applications [18]. Williams and Nievinski [19] studied the impact of tropospheric path delay on sea-level retrievals with a wide range of stations and identified a scale error due to a lack of a proper troposphere delay

correction. Nikolaidou et al. [20] quantitatively studied the tropospheric error for GNSS-IR using 3-D raytracing together with a standard atmosphere model. The study revealed that the GNSS-IR tropospheric error exhibits a linear dependence on reflector height and an exponential dependence on satellite elevation angle. These studies have focused on the characteristics of the tropospheric error and its impact on GNSS-IR sea-level retrievals, while the correction algorithm itself is not well studied. For example, many studies [19], [21], [22] assumed that the tropospheric error for the direct and reflected signals "cancels out" above the GNSS antenna. Furthermore, the sea surface is usually treated as a planar surface [19], [20], [23].

For GNSS-IR application studies, researchers have employed different strategies to address tropospheric errors. Some studies choose to apply both the bending angle and the path delay corrections [24], [25]. Some studies choose to apply only one of them [26], [27], and some studies choose to apply no tropospheric correction at all [14], [28], [29], [30], [31], [32]. The objective of this work is to develop a more comprehensive yet practical tropospheric error formula for GNSS-IR.

In Section II, we give the analytical deduction of the novel interferometric tropospheric error (NITE) formula for GNSS-IR, with a focus on sea-level monitoring. In Section III, the subcomponent and the total tropospheric error are validated using raytracing with radiosonde data. In Section IV, we present experimental assessment results of different tropospheric correction strategies using stations with different reflector heights. Section V discusses the relationship between the NITE formula and the previous approaches. In Section VI, we summarize this work and discuss the limitations of the NITE formula, addressing potential areas for further research and development.

II. GNSS-IR Tropospheric Error Formula

A. Geometry and Assumptions

Fig. 1 depicts the geometry for GNSS-IR considered in this work. The major assumptions are given as follows.

1) A spherical Earth with the Gaussian radius at the station.
2) The GNSS antenna is located $\leq$100 m above the sea.
3) The GNSS satellite is located at a far but finite distance.

The space from the sea surface to the satellite is divided into three layers. The first layer starts from the sea surface and extends up to the GNSS antenna. Since we limit the NITE formula to ground-based GNSS-IR, the first layer has a thickness of 100 m at maximum. The second layer begins at the GNSS antenna and reaches the top of the atmosphere, which is $\approx$100 km [33]. The third layer encompasses the region from the top of the atmosphere to the satellite, spanning over >20 000 km. The substantial difference in magnitudes allows us to apply some approximations without losing much accuracy.

As shown in Fig. 1, the reflected signal path is divided at the reflection point into a down-leg part and an up-leg part. The down-leg denotes the signal from the satellite to the reflection point. The up-leg goes from the reflection point to the GNSS antenna.

B. Geometric Displacement Error

In Fig. 1, the reflection point is displaced compared to a vacuum flat surface reflection. Atmospheric refraction, Earth's curvature, and the finite distance to the satellite all contribute to this displacement. In the following, we first obtain approximate expressions for the parameters that account for these effects; thus, the location of the reflection point is determined. After that, we derive the interferometric radio length for GNSS-IR considering the displaced reflection point.

In this section, we quantify only the straight-line geometric interferometric radio length. In Fig. 1, this is obtained in the dot-filled triangle as

$$\tau_i = L_{\text{down}} + L_{\text{up}} - G \tag{2}$$

where L_{down}, L_{up}, and G are the straight-line length of the down-leg, the up-leg, and the direct signal, respectively.

Due to the atmospheric refraction, the true signal path is curved; hence, the apparent elevation angle e_A at the antenna, also called the angle of arrival, is larger than the true elevation angle e_T, i.e.,

$$e_A = e_T + \Delta e \tag{3}$$

where Δe is the atmospheric bending angle. This bending angle has been extensively studied in astronomy, as angular observables are widely used in optical astronomy [34], [35]. Santamaría-Gómez and Watson [16] studied this bending angle on GNSS reflectometry and adopted an equation given by Bennett [17] as

$$\Delta e = \frac{510}{\frac{9}{5}T + 492}\,\frac{P}{1010.16}\cot\left(e_T + \frac{7.31}{e_T + 4.4}\right) \tag{4}$$

where T is the temperature in °C, P the pressure in hPa at the antenna, and e_T is the true elevation angle. Notice that (4) does not require the input of water vapor pressure. However, tropospheric water vapor is a major error contributor to GNSS signal propagation [36], [37], and the basis of GNSS meteorology [38], [39]. We take a similar equation given by Ulich [40], where the water vapor effect is considered. The Ulich equation is

$$\Delta e = 10^{-6} N \frac{\cos e_T}{\sin e_T + 0.00175\tan(87.5^\circ - e_T)} \tag{5}$$

where N is the ground refractivity in parts per million (ppm). The refractivity $N = 10^6(n-1)$, and n is the frequency-dependent atmospheric refractive index. For GNSS, the latest development of atmospheric refractivity is given by [41]

$$N = K_1\frac{P_d}{T} + K_2\frac{P_w}{T} + K_3\frac{P_w}{T^2} \tag{6}$$

where P_d and P_w are the dry and water vapor pressure in hPa and T is the temperature in kelvin. The coefficients are $K_1 = 77.6890$ (K/hPa), $K_2 = 71.2952$ (K/hPa), and $K_3 = 375\,463$ (K^2/hPa), respectively. We will always use the Ulich equation [see (5)] to calculate the bending angle Δe in the following deductions, except for the experiment part where we include the Bennett equation for comparison.

Due to Earth's curvature, the local vertical at the reflection point is rotated by an angle θ_E, which equals the angle formed

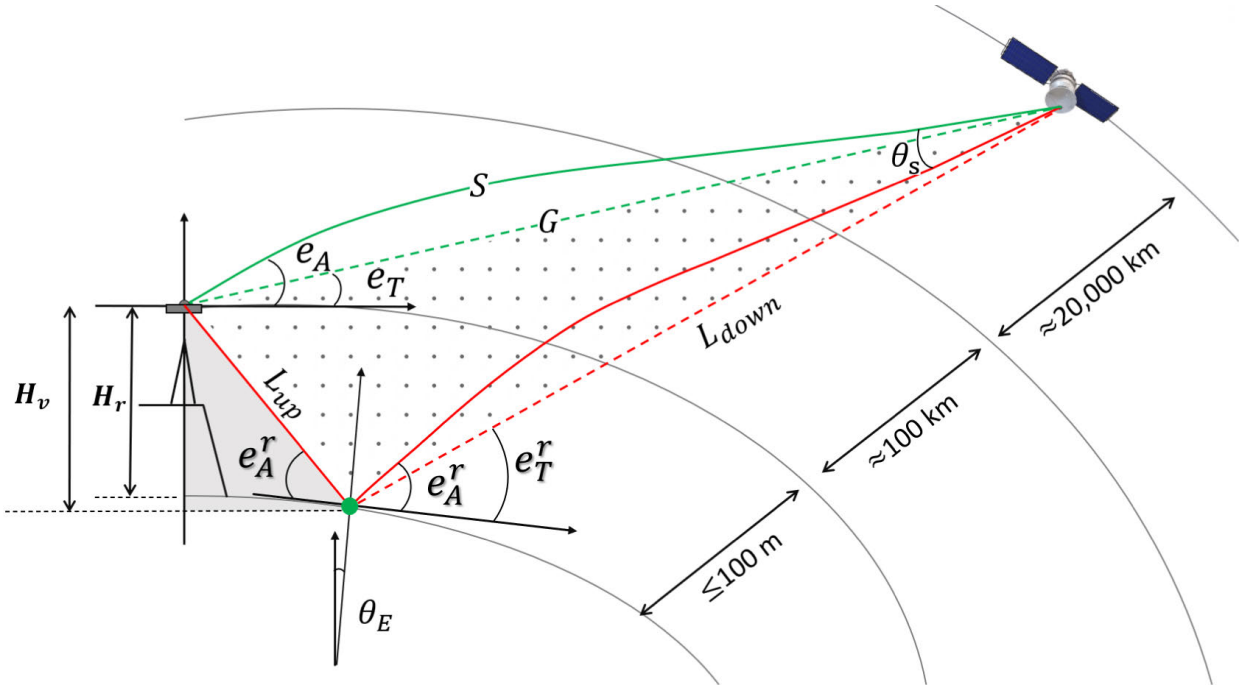

Fig. 1. Geometry of the setup of a coastal GNSS-IR station with atmospheric refraction and Earth's curvature (not to scale).

TABLE I

REFLECTION POINT VERTICAL DISPLACEMENT ($H_v - H_r$) IN cm, FOR DIFFERENT REFLECTOR HEIGHTS H_r, WITH $N_0 = 320$ ppm

H_r (m)	2°	3°	5°	7°	10°	20°	30°	80°
10	0.5	0.2	0.1	<0.1	<0.1	<0.1	<0.1	<0.1
20	1.9	1.0	0.4	0.2	0.1	<0.1	<0.1	<0.1
30	4.3	2.2	0.9	0.4	0.2	0.1	<0.1	<0.1
50	**11.9**	6.0	2.4	1.2	0.6	0.1	0.1	<0.1
100	47.7	24.2	**9.5**	5.0	2.5	0.6	0.2	<0.1

by the reflection point, Earth's center, and the antenna. For a spherical Earth, the reflection point is slightly lower than that of the "plane reflection" [42]. We define a vertical height H_v as the vertical distance between the reflection point and the antenna (see Fig. 1). Using the small angle approximation, we have

$$\begin{cases} \theta_E \approx \dfrac{H_r}{R \tan e_A} \\ H_v = H_r + R(1 - \cos\theta_E) \end{cases} \tag{7}$$

where R is the radius of the Earth. The reflection point vertical displacement will directly bias the reflector height H_r, and the magnitude is shown in Table I. The reflection point vertical displacement is about 1 cm for $H_r = 20$ m and $e_T = 3°$ and close to 12 cm for $H_r = 50$ m and $e_T = 2°$.

Due to the finite satellite distance, the direct and reflected signals form a small angle, marked as θ_S (see Fig. 1). Some studies showed that the impact of a finite satellite distance is negligible on GNSS signal propagation [43]. For GNSS satellites, the orbit radius is about 26 000 km; thus, L_{down} is about 23 700 ($e_T = 20°$) to 25 600 km ($e_T = 2°$), which corresponds to 3.7–4 times the Earth radius R. We keep the angle θ_S for completeness but adopt a rough approximation of L_{down} for current GNSS satellites. We have

$$\begin{cases} L_{\text{down}} \approx 4R \\ \theta_S = \dfrac{2H_r \cos e_A}{L_{\text{down}}}. \end{cases} \tag{8}$$

The derivations presented above give approximate expressions to quantify the atmospheric refraction (e_A, Δe), Earth's curvature effects (θ_E, H_v), and the effect due to the finite satellite distance (L_{down}, θ_S). With these parameters, the geometry between the antenna, the satellite, and the reflection point can be determined. Then, the reflector height H_r (H_v) can be related to the interferometric radio length τ_i by applying trigonometry in the shadowed and dot-filled triangles in Fig. 1. These two triangles share a common side, which is the up-leg L_{up}.

The down-leg resembles the direct signal but rotated by an angle θ_S. Together with the local vertical rotation θ_E, we can calculate the true elevation angle of the down-leg e_T^r from the true elevation angle of the direct signal e_T. Assuming the apparent elevation angle e_A^r differs from e_A by the same amount (approximation), we have

$$\begin{cases} e_T^r = e_T + \theta_E + \theta_S \\ e_A^r \approx e_A + \theta_E + \theta_S. \end{cases} \tag{9}$$

Applying Snell's law at the reflection point, the grazing angle of the up-leg equals that of the down-leg, which is the apparent elevation angle e_A^r (local tangential direction of the curved signal path). The up-leg is treated as a straight line and forms a right triangle (shadowed in Fig. 1) with H_v. Therefore, the length of the up-leg is

$$L_{\text{up}} = \frac{H_v}{\sin\left(e_A^r + \theta_E\right)}. \tag{10}$$

TABLE II

MAGNITUDE OF TRUE ELEVATION ANGLE e_T, APPARENT ELEVATION ANGLE e_A, EARTH'S CENTER ANGLE θ_E, AND SATELLITE ANGLE θ_S, FOR DIFFERENT REFLECTOR HEIGHTS H_r, WITH $N_0 = 320$ ppm

	e_T (e_A)					
	2° (2.32°)		5° (5.18°)		10° (10.10°)	
H_r(m)	θ_E	θ_S	θ_E	θ_S	θ_E	θ_S
10	$2.2e^{-3}$	$4.5e^{-5}$	$9.9e^{-4}$	$4.5e^{-5}$	$5.0e^{-4}$	$4.4e^{-5}$
20	$4.5e^{-3}$	$9.0e^{-5}$	$2.0e^{-3}$	$8.9e^{-5}$	$1.0e^{-3}$	$8.8e^{-5}$
30	$6.6e^{-3}$	$1.3e^{-4}$	$3.0e^{-3}$	$1.3e^{-4}$	$1.5e^{-3}$	$1.3e^{-4}$
50	$1.1e^{-2}$	$2.2e^{-4}$	$5.0e^{-3}$	$2.2e^{-4}$	$2.5e^{-3}$	$2.2e^{-4}$
100	$2.2e^{-2}$	$4.5e^{-4}$	$9.9e^{-3}$	$4.5e^{-4}$	$5.0e^{-3}$	$4.4e^{-4}$

Notice that the satellite is far away and θ_S is small. Equation (2) can be approximated as the up-leg minus its projection on the direct signal direction

$$\tau_i = \frac{H_v}{\sin\left(e_A^r + \theta_E\right)}\left(1 - \cos\left(e_T + e_A^r + \theta_E\right)\right). \tag{11}$$

The term $L_{\text{down}}(1 - \cos\theta_S)$ is ignored because of its small magnitude (~0.8 mm for $H_r = 100$ m and $e_T = 2°$). The difference between (11) and (1) is the geometric displacement error of the NITE formula. The geometric displacement error accounts for the displacement of the reflection point.

When the true elevation angle is large, the atmospheric bending angle Δe will be small; thus, we have ($e_A^r \approx e_T$, $\theta_E \approx 0$), and (11) will simplify to

$$\tau_i = H_v \frac{1 - \cos(2e_T)}{\sin(e_T)} = 2H_v \sin e_T. \tag{12}$$

When the true elevation angle is large and the antenna is close to the sea surface, (11) becomes (1).

In Table II, we can see that $e_A > 100\,\theta_E > 1000\,\theta_S$. This relationship facilitates certain approximations in the derivation. Equation (7) is obtained using the small angle approximation. In (8), θ_S is obtained in a similar manner. The justification behind these approximations is that, while not exact, θ_E and θ_S provide a reasonably accurate representation of their evolving trends with respect to elevation angles, which is critical for SNR-based GNSS-IR [19].

In addition to the bending angle, the atmospheric refraction also caused an extra curve path effect. The curve path effect is identical in GNSS positioning and is included in all commonly used mapping function products [44]. In Section II-C, when we derive the interferometric tropospheric path delay, this interferometric curve path effect will be covered.

C. Interferometric Tropospheric Path Delay

In this section, we quantify the interferometric tropospheric path delay for GNSS-IR. The up-leg is treated as a straight line; thus, the path delay is the length multiplied by the average refractivity. The path delay for the direct signal is identical to that of the GNSS positioning applications. The down-leg of the reflected signal resembles the direct signal; therefore, the path delay is evaluated similarly.

We start the deduction of the path delay by first defining the interferometric tropospheric path delay of GNSS-IR. The interferometric path delay is the difference between the tropospheric delay experienced by the reflected and the direct GNSS signal

$$D_i = D_{\text{up}} + D_{\text{down}} - D_d \tag{13}$$

where D_{up}, D_{down}, and D_d represent the tropospheric delay of the reflected up-leg, the reflected down-leg, and the direct path, respectively.

We then define an average layer refractivity N_l, which is representative of the layer between the GNSS antenna to the reflecting surface. It can be calculated as

$$N_l = N_0 \frac{1 + e^{\frac{H_r}{8000}}}{2} \tag{14}$$

where N_0 is the refractivity measured at the GNSS antenna. Equation (14) simply gives the arithmetic average refractivity of the top (antenna) and bottom (reflecting surface) of this thin layer, assuming an exponential refractivity profile with a fixed scale height of 8000 m. Another choice would be the average of the refractivity in this layer as a continuous function. For an antenna that is 100 m above the sea surface, these two approaches differ by less than 0.004 ppm.

The up-leg path is relatively small, and the length is given in (10). The tropospheric delay of the reflected signal up-leg can be obtained by multiplying the average layer refractivity and the up-leg length as

$$D_{\text{up}} = 10^{-6} N_l \frac{H_v}{\sin\left(e_A^r + \theta_E\right)}. \tag{15}$$

The direct signal path delay caused by the atmosphere is identical to that in usual GNSS positioning, and it is evaluated accordingly. The radio signal is retarded due to the atmosphere refractivity, and this is usually referred to as the tropospheric delay [45], [46]. The tropospheric delay is an important error source of GNSS and has been well-studied in positioning applications. Thanks to the developments of numerical weather models and high-performance computing, we now have state-of-art mapping function products available for the correction of tropospheric effects [37], [47]. With the predetermined value of mapping functions, GNSS can estimate the zenith total delay (ZTD) and, in return, contribute to meteorology studies. We use the mapping function developed for GNSS positioning, and we also use the information of the upper part of the atmosphere (ZTD) obtained by the GNSS meteorology method to deduce the tropospheric path delay for GNSS-IR.

According to the definition, the direct signal path delay is

$$D_d = \int_{\text{ant}}^{\text{sat}} (n - 1) ds + (S - G) \tag{16}$$

where n is the refraction index along the curved signal path and $(S - G)$ is the differential length between the true curved signal path and the straight line, i.e., the curved path effect (see Fig. 1). The curve path effect is <2% of the tropospheric delay.

Equation (16) can be used to calculate accurate tropospheric delay via a raytracing method and generate mapping functions, while in GNSS data processing, the tropospheric delay is then

modeled as [46], [48]

$$D_d = \mathrm{ZTD} \cdot \mathrm{mpf}(e_T). \tag{17}$$

Here, ZTD is the zenith total delay and $\mathrm{mpf}(e_T)$ is the elevation angle dependent total mapping function.

The tropospheric path delay of the reflected signal down-leg is evaluated in a similar way as

$$D_{\mathrm{down}} = (\mathrm{ZTD} + \mathrm{ZTD}_l) \cdot \mathrm{mpf}\left(e_T^r\right) \tag{18}$$

where ZTD_l is the "layer ZTD" between the GNSS antenna and the reflector surface as $\mathrm{ZTD}_l = 10^{-6} N_l H_r$. Comparing (18) and (17), they are both applying the definition of the mapping function. The mapping function value for the reflected down-leg signal differs slightly from that of the direct signal for two reasons. First, the mapping function is a function of station height. Second, the true elevation angles e_T^r and e_T are not identical.

A height correction is needed for sites at different altitudes when applying the mapping function [43], [49]. The height correction for the hydrostatic mapping function given by Niell [36] can be written as

$$\frac{\partial \mathrm{mpf}}{\partial h} = \frac{1}{\sin e_T} - \frac{1 + \frac{a}{1+\frac{b}{1+c}}}{\sin e_T + \frac{a}{\sin e_T + \frac{b}{\sin e_T + c}}} \tag{19}$$

where $a = 0.0000253$, $b = 0.00549$, and $c = 0.00114$. The accuracy of the mapping function height correction given by (19) has been questioned [43], [49]. A more accurate height correction can be realized by numerical methods that involve using raytracing to obtain mapping function at multiple altitudes at a global scale, with a fine enough numerical weather model. That is out of the scope of this work. As we limit the NITE formula for ground-based GNSS-IR with a maximum reflector height of 100 m, numerical results show that the height correction term is secondary compared to the effects of the true elevation angle difference.

The effect caused by the true elevation angle difference is quantified with the help of the partial derivative of the mapping function with respect to the true elevation angle. The mapping function is usually expressed as a parameterized continued fraction. The partial derivative of the mapping function can be analytically expressed as

$$\frac{\partial \mathrm{mpf}}{\partial e_T} = \left(\frac{a\left(\cos e_T - \frac{b \cos e_T}{(c+\sin e_T)^2}\right)}{\left(\frac{b}{c+\sin e_T} + \sin e_T\right)^2} - \cos e_T \right) \cdot \mathrm{mpf}(e_T) \tag{20}$$

with a, b, and c being the mapping function products [50]. In practice, this partial derivative can also be numerically calculated by first calculating the mapping function at two slightly different elevation angles. An implementation of (20) is included in the code to use the global mapping function (GMF) product available at [51].

The true elevation angle difference between the direct and reflected signal down-leg paths is available in (9) as $\Delta e_T = e_T^r - e_T = \theta_E + \theta_S$. Now, (18) can be written as

$$D_{\mathrm{down}} = (\mathrm{ZTD} + \mathrm{ZTD}_l) \cdot \left[\mathrm{mpf}(e_T) - \left(\frac{\partial \mathrm{mpf}}{\partial e_T} \Delta e_T + \frac{\partial \mathrm{mpf}}{\partial h} H_r \right) \right]. \tag{21}$$

Consider that ZTD_l is small compared to ZTD [for an antenna of 100 m distance to the sea surface, $\mathrm{ZTD}_l \approx (\mathrm{ZTD}/80)$] and the same situation stands for the mapping function and its differences. Combining (15) and (21) and subtracting the direct signal tropospheric delay by (17), the interferometric tropospheric path delay of GNSS-IR is

$$D_i = \frac{10^{-6} N_l H_v}{\sin\left(e_A^r + \theta_E\right)} + 10^{-6} N_l H_r \mathrm{mpf}(e_T) - \mathrm{ZTD}\left(\frac{\partial \mathrm{mpf}}{\partial e_T} \Delta e_T + \frac{\partial \mathrm{mpf}}{\partial h} H_r \right). \tag{22}$$

Equation (22) gives the interferometric tropospheric path delay of GNSS-IR as a function of the reflector height $H_r(H_v)$, the average layer refractivity N_l, the true elevation angle e_T, the ZTD, and the mapping function and its partial derivative. Although (22) is complicated, the only required observable data are the refractivity at the antenna, i.e., meteorology data. ZTDs are always estimated together with the position in high-precision GNSS data processing. GNSS-estimated ZTDs typically range from 2.2 to 2.6 m, with an accuracy of better than 1 cm [52] and a temporal resolution of up to 5 min. Equation (22) is the interferometric path delay of the NITE formula.

While (22) gives the interferometric tropospheric path delay in the form of forward modeling, it is challenging to directly apply it, especially for the SNR-based GNSS-IR. The issue lies in Earth's curvature effect, which is expressed in (7) and depends on the reflector height (H_r) with an ${H_r}^2$ term. We adopt a simple first-order correction by introducing an H_v to H_r ratio K expressed as

$$K = \frac{H_v}{H_r} \approx 1 + \frac{H_r^0}{2R \tan^2 e_A} \tag{23}$$

where H_r^0 is an a priori value of H_r. This value does not need to be known very accurately for normal ground-based GNSS-IR. Alternatively, it can be solved iteratively if H_r changes dramatically [53]. Combining (11) and (22) and inserting K, we can extract the reflector height H_r term to obtain an equation suitable to be applied to (1) directly at the observable level using a variable substitute method [15] as

$$\tau_i = H_r \left[K \frac{1 - \cos\left(e_T + e_A^r + \theta_E\right)}{\sin\left(e_A^r + \theta_E\right)} + K \frac{10^{-6} N_l}{\sin\left(e_A^r + \theta_E\right)} + 10^{-6} N_l \mathrm{mpf}(e_T) - \mathrm{ZTD} \times \left(\frac{\partial \mathrm{mpf}}{\partial e_T} \frac{1 + 0.5 \sin e_A}{R \tan e_A} + \frac{\partial \mathrm{mpf}}{\partial h} \right) \right]. \tag{24}$$

III. Raytracing Validation

A. Subcomponents of the Tropospheric Error

We use raytracing to validate the geometric displacement error and the path delay from the NITE formula. The two-step 2-D raytracing method for GNSS-IR is documented in the

TABLE III
RADIOSONDE STATIONS FOR RAYTRACING VALIDATION

Radiosonde station	Latitude (°)	Longitude (°)	Height (m)	Nearby GNSS
FPM00091938	−17.5550	−149.6200	2.0	FAA1
ASM00094672	−34.9525	138.5203	6.1	SPRB
GRM00016754	35.3353	25.1819	35.0	NOMI
USM00072327	36.2472	−86.5631	180.2	KYDH
USM00072469	39.7675	−104.8694	1611.0	P041
ASM00094975	−42.8339	147.5033	4.0	BUR2
SPM00008023	43.4911	−3.8006	52.0	SCOA
USM00072797	47.9339	−124.5603	56.8	SC02
FRM00007110	48.4442	−4.4119	99.0	BRST
SWM00002527	57.6572	12.2911	164.0	OSOU
USM00070326	58.6811	−156.6514	8.4	PBAY
AYM00089571	−68.5740	77.9672	18.0	DAV1
AYM00089532	−69.0050	39.5811	18.4	SYOG
SVM00001004	78.9233	11.9222	15.5	NYA2

Appendix. This raytracing algorithm considers the curvature of the Earth and the finite distance of GNSS satellites. Radiosondes profiles [54] are used as realistic samples to evaluate the consistency between the NITE formula and numerical raytracing. In the upper part of the atmosphere where radiosonde data are not available, we extend the profile up to 100 km with a standard atmospheric model [55]. In total, 14 globally distributed radiosonde stations were selected, following previous GNSS-IR studies [56] but also covering a wide range of climate regions, including Antarctica [26]. Information of radiosonde stations together with the four-digit name of nearby GNSS stations are presented in Table III.

The interferometric radio length assuming a vacuum and plane reflection is given by (1). We use (1) as the baseline value and refer to it as the $\sin e_T$ model. Equation (11) (NITE geometric formula) differs from (1) as we considered the reflection point change due to the atmosphere and Earth's curvature. The difference between (11) and (1) is the NITE geometric displacement error.

In Fig. 2, the NITE geometric displacement error is compared to raytracing values. The $\sin e_T$ model was used as the baseline value. Therefore, it is shown as zero in Fig. 2. Results for reflector heights of 20 and 100 m are presented, and the ground refractivity was chosen to be 320 ppm (average summer condition in Gothenburg, Sweden). The geometric displacement error of the NITE formula agrees well with raytracing. For $H_r = 20$ m and $e_T = 2°$, the geometric displacement error from raytracing is ≈1 cm. The NITE geometric formula given by (11) differs from raytracing at the level of < 1 mm. For $H_r = 100$ m and $e_T = 2°$, the geometric displacement error from raytracing is ≈8 cm, and the NITE geometric formula has an error of ≈3 mm. The error of the NITE geometric formula increases when the reflector height increases or when the elevation angle decreases. The fact that the $\sin e_T$ model and raytracing only have differences of about 1 cm for $H_r = 20$ m and $e_T = 2°$ means that the geometric displacement error is very small.

The NITE geometric formula given by (11) might be confused with the "bending angle correction" used in [16], as they both rely on the apparent elevation angle. However, they are very different both in physical meaning and magnitude. With

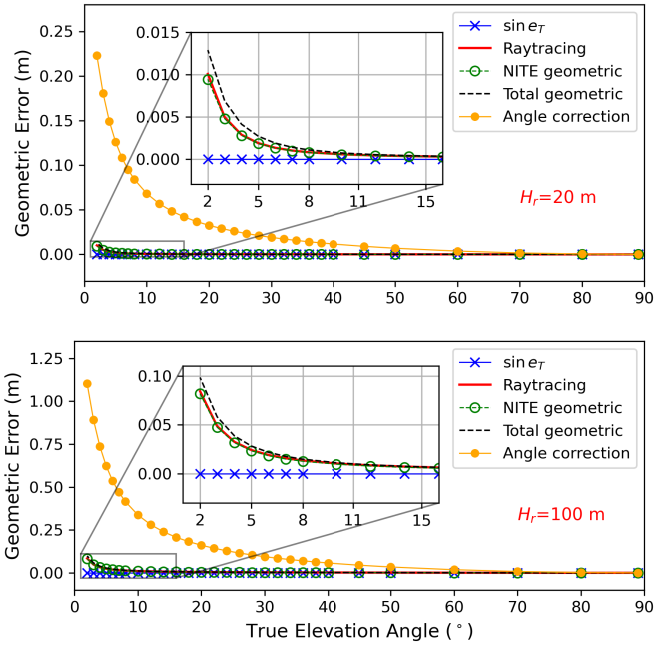

Fig. 2. NITE geometric displacement error compared to raytracing (zoomed-in part). The vacuum τ_i ($\sin e_T$) was subtracted. The results are presented for two reflector heights (top) $H_r = 20$ m and (bottom) $H_r = 100$ m, with a refractivity of 320 ppm at the antenna. The black dashed line shows the total geometric error (geometric displacement error plus the curve path effect).

the "bending angle correction," the true elevation angle in (1) was replaced by the apparent elevation angle as

$$\tau_i = 2H_r \sin e_A. \tag{25}$$

Therefore, the value of the (bending) angle correction is $\Delta\tau_i = 2H_r(\sin e_A - \sin e_T)$, which is also presented in Fig. 2 (orange line with solid dots). As we can see, the bending angle correction gives a much larger correction value. The total interferometric tropospheric geometric error (geometric displacement error plus the curve path effect) is plotted in Fig. 2 with a black dashed line. The curved path effect is about 3 mm ($H_r = 20$ m and $e_T = 2°$) to 1 cm ($H_r = 100$ m and $e_T = 2°$). Even if the curved path effect is added, the bending angle correction will still not match the total interferometric tropospheric geometric error. The bending angle correction by Santamaría-Gómez and Watson [16] is not correcting the geometric part of the tropospheric error.

The $\sin e_T$ model follows a vacuum medium and a plane reflector propagation. However, the troposphere refraction does impact the signal path and contributes to the geometric displacement error. In Fig. 3, the geometric displacement errors (not just the troposphere) from raytracing and model values for $H_r = 20$ m and $e_T = 2°$ are plotted versus ground refractivity using data from all the 14 sites. We can see from the raytracing results that the geometric displacement error changes with the ground refractivity, and the NITE geometric formula given by (11) fits the relation well. The $\sin e_T$ model, however, does not respond to ground refractivity variation. In our dataset, the ground refractivity ranges from 240 to 400 ppm, but the ground refractivity for a specific location only covers part of this range. Using the $\sin e_T$ model

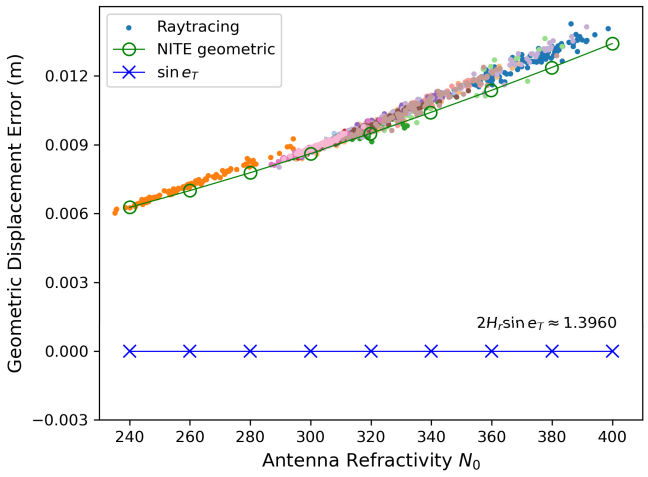

Fig. 3. GNSS-IR geometric displacement error versus GNSS antenna refractivity from raytracing (solid dots), the vacuum-based $\sin e_T$ model (blue crosses), and the NITE formula (green circles) for reflector height $H_r = 20$ m and elevation angle $e_T = 2°$. The plot uses radiosonde data from 14 globally distributed sites (in different colors).

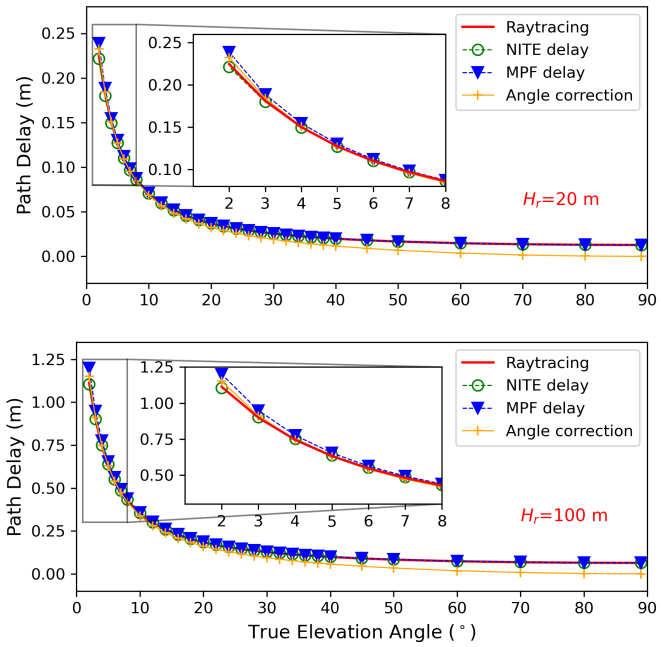

Fig. 4. Interferometric tropospheric path delay from raytracing and different approaches using a radiosonde profile with ground refractivity of 320 ppm.

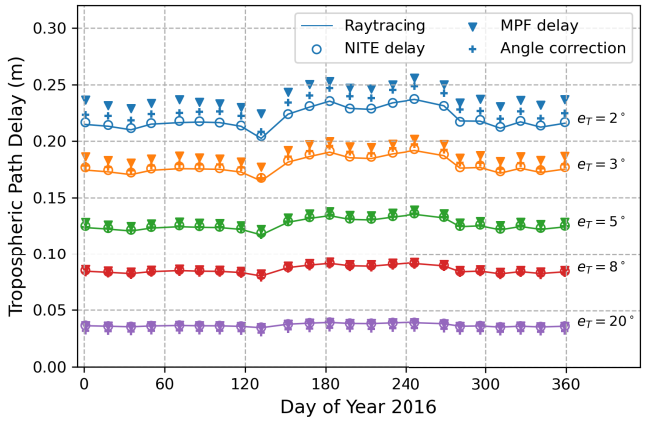

Fig. 5. One-year time series of tropospheric path delay of different approaches compared to raytracing with radiosonde data near Gothenburg, Sweden; $H_r = 20$ m.

to describe the interferometric radio length will introduce inhomogeneous errors for different locations.

For the interferometric tropospheric path delay, previously, some studies [19] used an approach to correct the tropospheric path delay directly using a mapping function as the slant factor. This assumes that the path delays for the direct and reflected signals cancel out above the antenna, and a mapping function is used to map the "layer ZTD" to different elevation angles. We will refer to it as the "mapping function path delay (MPF delay)" approach

$$D_i = 2 \cdot 10^{-6} H_r N_l \,\mathrm{mpf}(e_T). \tag{26}$$

However, the "cancels out above the antenna" assumption to some degree contradicts the use of a mapping function as the slant factor because a mapping function is determined for the whole atmosphere up to 80 km [37].

Fig. 4 depicts an example of interferometric tropospheric path delay over elevation angles from the MPF delay approach, the NITE path delay, and the reference value from raytracing. The refractivity profile is derived from radiosonde data on a summer day in the Gothenburg-Landvetter Airport, Landvetter, Sweden, with a ground refractivity of 320 ppm. For the MPF and NITE path delay formulas, we use the GMF mapping function as input. For two reflector heights of 20 m (top) and 100 m (bottom), the NITE path delay [see (22)] gives almost identical values as raytracing. The MPF delay approach gives a slightly larger path delay than raytracing. For elevation angle $> 15°$, the differences between the MPF delay approach, the NITE formula, and the raytracing path delay are very small. The bending angle correction is also plotted in Fig. 4. The bending angle correction gives a correction that is overall very close to the interferometric tropospheric path delay. However, in the zenith direction, the apparent and the true elevation angles are equal, which means no tropospheric correction with the bending angle correction.

Comparing the y-axis range of Figs. 2 and 4, it is clear that the path delay is the major part of the GNSS-IR tropospheric error. For an antenna of 20 m height above the sea surface, the geometric displacement error is <5% of the path delay at 2°, and at high elevation angles, the geometric displacement error decreases to zero but not the path delay.

Fig. 5 gives one-year time series of GNSS-IR tropospheric path delay obtained from the bending angle correction, the MPF delay, and the NITE formula for $H_r = 20$ m and $e_T = 2°, 3°, 5°, 8°, 20°$. Despite the radiosonde data coming from a location with noticeable seasonal variations (southern Sweden), the GNSS-IR tropospheric delay exhibits only minor fluctuations throughout the year. The NITE formula gives the closest results to raytracing. The MPF delay approach has a small positive bias. Interestingly, at 2°, the bending angle correction appears to compensate for the tropospheric **path delay** better than the MPF delay approach.

B. Total Tropospheric Error Validation

Regardless of the definition of each subcomponent, in practice, it is the total tropospheric error that affects the observations. In this section, we validate the total tropospheric error given by the bending angle correction, the MPF delay, and the NITE formula. For the bending angle correction, the GNSS-IR interferometric radio length τ_i is given by (25). For the MPF delay approach, the interferometric radio length is the sum of (1) and (26). For the NITE formula, the interferometric radio length is the sum of (11) and (22).

The total tropospheric error from these three approaches was validated using raytracing. One year of radiosonde data from 14 global stations (see Table III) was used, but only two profiles were used every 30 days. The average model errors for the three approaches are presented in Fig. 6. Detailed numerical values are given in Table IV. On the left-hand side of Fig. 6, the total tropospheric delay model errors are given for reflector height from 5 to 50 m for $e_T = 2°$. The right-hand side of Fig. 6 is for $e_T = 5°$ and H_r from 10 to 100 m. In the upper row, the GMF [57] and N_l from (14) were used as input. The model bias with 1σ standard deviation is plotted. It can be observed that the NITE formula demonstrates the best performance, followed by the MPF delay. The MPF delay tends to overestimate the total tropospheric error, while the bending angle correction underestimates the total tropospheric error. The NITE formula also has smaller σ compared to the other two approaches, which means that the NITE formula is able to capture the variation of the total tropospheric error better, for different locations and times. For $e_T = 5°$, both MPF and NITE formulas exhibit minimal errors compared to raytracing. The NITE formula has a negative bias and the bias increases with reflector height (H_r) almost linearly (see Table IV).

Both the MPF delay and the NITE formula require the input of mapping function values and an average layer refractivity N_l. The accuracy of the mapping functions and N_l will impact their accuracy. In the middle row in Fig. 6, the mapping function was generated from the corresponding radiosonde profile, i.e., an ideal mapping function. In the lower row, both the mapping function and N_l were generated from the corresponding radiosonde profile. Comparing the middle and upper rows, we can see that the bias of the NITE formula is almost removed with the "perfect" mapping function input, while the MPF delay does not benefit much from the better mapping function values. Comparing the lower row and the middle row, we can see that the NITE formula now produces nearly identical values as raytracing. This indicates that N_l given by (14) is the origin of random errors for the NITE formula. These random errors increase with the reflector height H_r. This is not surprising as (14) essentially solves the average layer refractivity below the GNSS antenna with the refractivity at the antenna only. In the lower rows, with the ideal N_l, the random errors (σ) of the MPF delay are also reduced. The lower row of Fig. 6 shows that the NITE formula exhibits excellent formal precision. However, in practical applications, the NITE formula will be limited by the accuracy of existing mapping function products and the representativeness of N_l.

The mapping function can be optimized at lower elevation angles for GNSS-IR application, considering that the GMF products adopted in this study are designed for $e_T > 3°$. We checked these 14 stations separately (not shown) and the biases of the NITE formula with GMF as input are similar across all stations though the weather conditions vary greatly. However, it is difficult to have a much better equation than (14) for the average layer refractivity when H_r increases. For more accurate tropospheric error correction, it is advisable to avoid excessively large reflector heights in GNSS-IR. Furthermore, the fact that the uncertainty in N_l contributes significantly to the random error suggests that there is a possibility to estimate the average layer refractivity together with the sea level, similar to the approach for estimating GNSS ZTD [58].

IV. Experimental Validation

In this section, we test and compare the tropospheric correction approaches discussed earlier with experiments. We collected GNSS and meteorology data for five stations from the day of year (DOY) 1, 2021, to DOY 180, 2022. Information about these five GNSS-IR stations is provided in Table V.

These five stations have nearly complete 1-Hz data records from the beginning of 2021 till the middle of 2022, and they also provide usable SNR data for the GNSS-IR study with relatively large elevation angle coverage. We also obtained high temporal resolution (≈10 min) meteorology and tide gauge data for these five sites.

Unfortunately, we were unable to find nearby tide gauge data for AT01. We include AT01 because it offers excellent elevation angle coverage for GNSS-IR applications, and the first experiment does not require the use of tide gauge data. The SC02 has a similar reflector height as OSOU but less usable elevation angle coverage. Therefore, SC02 was not used in the first experiment, and AT01 was not used in the second experiment.

We used the *gnssrefl* software [18], [59] for data processing. The GMB precise orbit products were employed to generate the true elevation angle. We used 5-s SNR data for OSOU and SC02, 2-s SNR for AT01, and 1-s SNR for ELLY and NYA2. The *gnssrefl* software currently only supports the bending angle correction with the Bennett equation. Tropospheric correction within the software was disabled.

Instead, we applied tropospheric corrections to the elevation angles of the SNR records using a variable substitute method [15]. Apart from the pressure, temperature, and humidity data, the NITE formula also incorporates the ZTD as input. The 5-min ZTD values for the five stations were obtained using the Automatic Precise Positioning Service provided by the Jet Propulsion Laboratory [60]. The hydrostatic and wet parts of GMF were weighted using zenith hydrostatic and wet delays to derive the total mapping function for input. The height rate correction [9] was also applied. Fig. 7 gives the procedure of the GNSS-IR processing with the NITE formula.

We tested six tropospheric correction strategies: (a) "angle Bennett," applying the bending angle correction with the Bennett equation; (b) "MPF," applying only the path delay with the MPF delay; (c) "angle Ulich," applying the bending

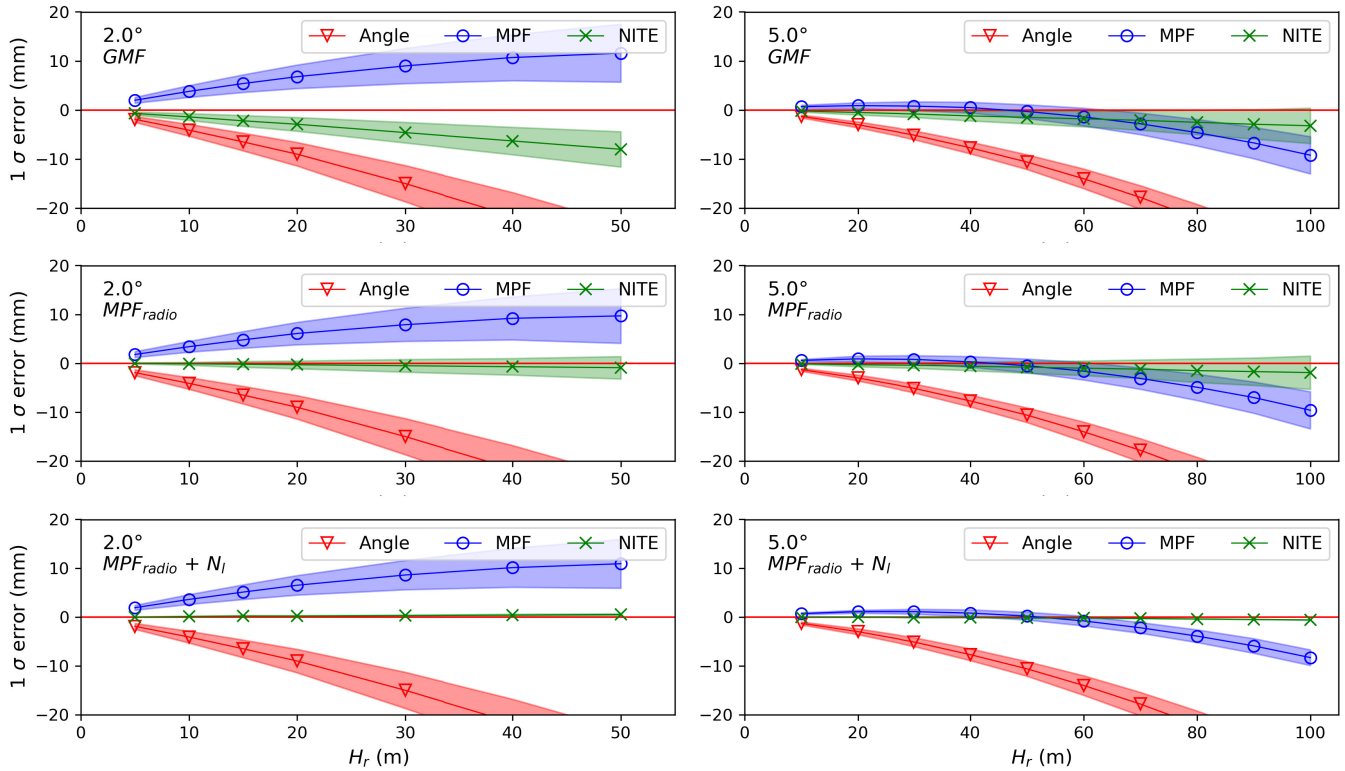

Fig. 6. Tropospheric total delay formula error at different reflector heights for (left) $e_T = 2°$ and (right) $e_T = 5°$. Upper row: with GMF as input. Middle row: with mapping function derived from corresponding radiosonde profile as input. Lower row: with mapping function and layer refractivity N_l from the corresponding radiosonde profile as input. Notice the different x-axis range for $e_T = 2°$ (left column) and $e_T = 5°$ (right column).

TABLE IV

TROPOSPHERIC TOTAL DELAY FORMULA ERROR IN mm (BIAS AND STANDARD DEVIATION) COMPARED TO RAYTRACING, AT DIFFERENT REFLECTOR HEIGHTS H_r, FOR $e_T = 2°$ AND $e_T = 5°$

	$e_T = 2°$				
Model Input	H_r	5 m	10 m	20 m	50 m
GMF	Angle	−1.9 (0.6)	−4.1 (1.2)	−9.0 (2.4)	−29.1 (6.0)
	MPF	+2.0 (0.6)	+3.8 (1.2)	+6.8 (2.4)	+11.6 (5.9)
	NITE	−0.7 (0.3)	−1.4 (0.7)	−2.9 (1.4)	−8.0 (3.6)
MPF_{radio}	Angle	−1.9 (0.6)	−4.1 (1.2)	−9.0 (2.4)	**−29.1** (6.0)
	MPF	+1.8 (0.6)	+3.4 (1.1)	+6.1 (2.3)	**+9.7** (5.6)
	NITE	< 0.1 (0.1)	−0.1 (0.3)	−0.3 (0.8)	**−0.9** (2.3)
MPF_{radio} N_l	Angle	−1.9 (0.6)	−4.1 (1.2)	−9.0 (2.4)	−29.1 (**6.0**)
	MPF	+1.9 (0.5)	+3.6 (1.0)	+6.5 (2.0)	+10.9 (**5.0**)
	NITE	< 0.1 (<0.1)	< 0.1 (<0.1)	+0.2 (0.1)	+0.5 (**0.2**)

	$e_T = 5°$				
Model Input	H_r	10 m	20 m	50 m	100 m
GMF	Angle	−1.3 (0.3)	−3.0 (0.6)	−7.7 (1.5)	−31.8 (4.0)
	MPF	+0.7 (0.3)	+0.9 (0.6)	−0.3 (1.4)	−9.2 (3.8)
	NITE	−0.2 (0.2)	−0.5 (0.5)	−1.5 (1.3)	−3.2 (3.6)
MPF_{radio}	Angle	−1.3 (0.3)	−3.0 (0.6)	**−7.7** (1.5)	−31.8 (4.0)
	MPF	+0.6 (0.2)	+0.9 (0.6)	**−0.5** (1.4)	−9.6 (3.8)
	NITE	−0.1 (0.1)	−0.3 (0.4)	**−0.8** (1.2)	−1.9 (3.4)
MPF_{radio} N_l	Angle	−1.3 (0.3)	−3.0 (0.6)	−7.7 (**1.5**)	−31.8 (4.0)
	MPF	+0.7 (0.2)	+1.1 (0.3)	+0.2 (**0.8**)	−8.3 (1.6)
	NITE	<0.1(<0.1)	<0.1(<0.1)	−0.2 (<**0.1**)	−0.6 (<0.1)

angle correction with the Ulich equation; (d) "NITE," applying the displacement and path delay error given by (11) and (22); (e) "no troposphere"; no tropospheric correction was applied; and (f) "angle + MPF," applying the bending angle correction using the Ulich equation together with the path delay correction with the MPF delay.

TABLE V
INFORMATION FOR THE FIVE GNSS-IR STATIONS

Station	H_r (m)	Lat (°)	Long (°)	Azimuth mask (°)	Elevation Range Nodes (°)
OSOU	3.7	57.393	11.914	70–260	2∼8∼15∼22.6∼32
SC02	5.5	48.546	−123.007	25–230	2∼7
AT01	13	63.484	−162.006	20–220	2∼5.4∼9 ∼13∼17
ELLY	33	33.583	−118.129	80–170, 210–310	2∼4.2∼6.5∼8.7∼13
NYA2	48	78.930	11.859	25–100	2∼4.2∼6.5∼8.7∼12

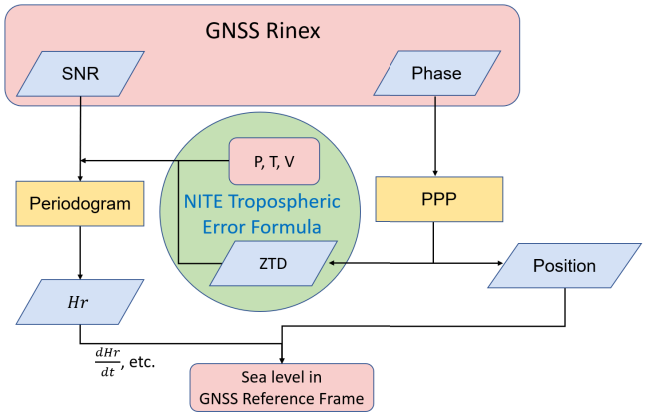

Fig. 7. GNSS-IR sea-level retrieval with the NITE formula.

A. Elevation Angle Range Test

First, we conducted an elevation angle range test. Tropospheric errors decrease rapidly when elevation angle increases; therefore, results from high elevation angle data are close to "tropospheric error free." By comparing results from low and high elevation angles, one can evaluate the performance of a troposphere correction strategy. We cut the SNR data into different elevation ranges. The elevation range cutting nodes were obtained individually for each station by dividing the elevation range between 2° and 30° into two, three, four, five, six, and so on average parts (sine value). Then, we chose the elevation angle cut strategy that has the most nodes, yet enough H_r solutions pass the quality check [18]. For example, for OSOU, we performed the GNSS-IR processing with elevation ranges of 2°–8°, 8°–15°, 15°–22.6°, and 22.6°–32°. The elevation angle cut strategy, along with the azimuth mask, is presented in Table V. This method is similar to the elevation angle truncate test described in the literature [61] or the sliding window method used by Williams and Nievinski [19]. However, in our approach, there is no overlap between different ranges so that each solution remains independent.

Fig. 8 gives a seven-day H_r time series of the elevation range cutting experiment for NYA2. H_r from all four elevation ranges varies in similar patterns, confirming the effectiveness of this elevation cut strategy. One advantage of this approach is that in stations where elevation angle coverage is good (AT01), the number of H_r retrievals can be improved by three to four times, resulting in better temporal resolution. Probably due to wave conditions, SNR data from higher elevation angles for ELLY was of poor quality for the year 2021. In total, 180 days of data from DOY 1, 2022, were used in this elevation angle range experiment.

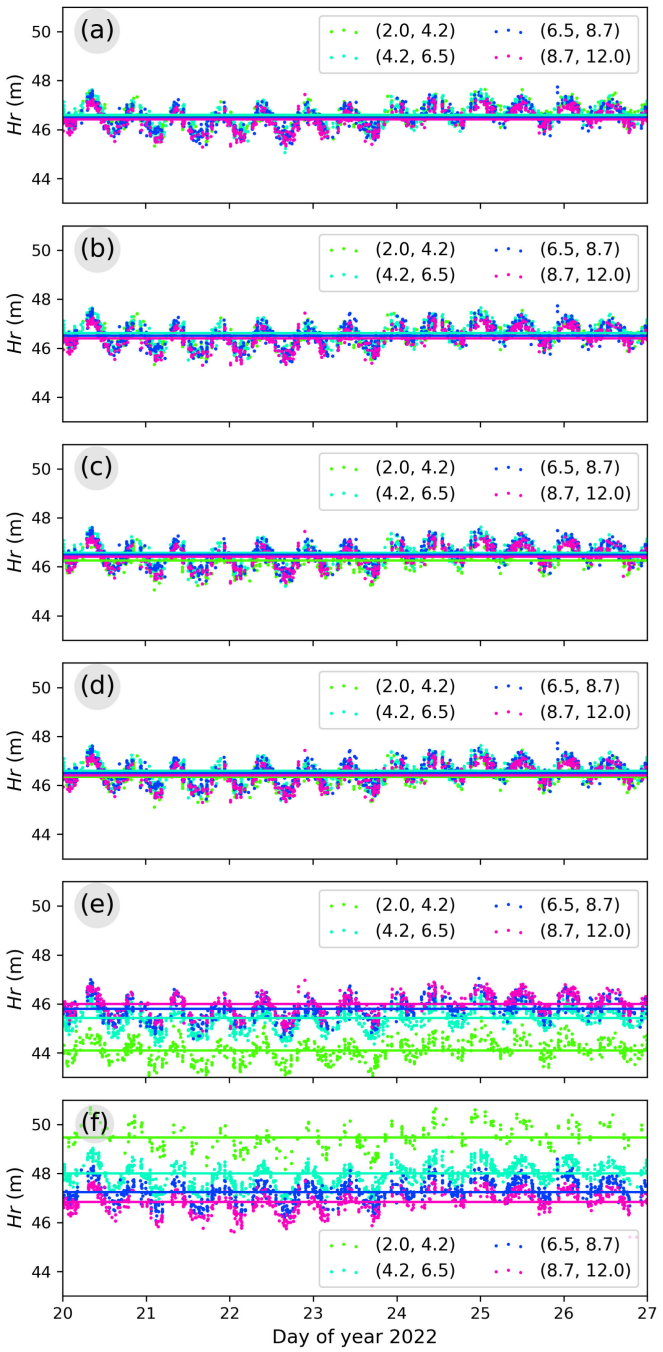

Fig. 8. Seven-day reflector height time series of NYA2 using data at different elevation angle ranges (in different colors) with six different tropospheric correction strategies: (a) angle Bennett, (b) MPF, (c) angle Ulich, (d) NITE, (e) no troposphere, and (f) angle + MPF.

The tropospheric error exhibits some variation over time. This variability is smaller but significant compared to the overall error (see Fig. 5). Observations at higher elevation angles are less affected by the tropospheric error, while observations at lower elevation angles are more susceptible to its influence. As a result, without correcting the tropospheric error, H_r retrievals from low and high elevation angle data will display nearly constant discrepancies in the time

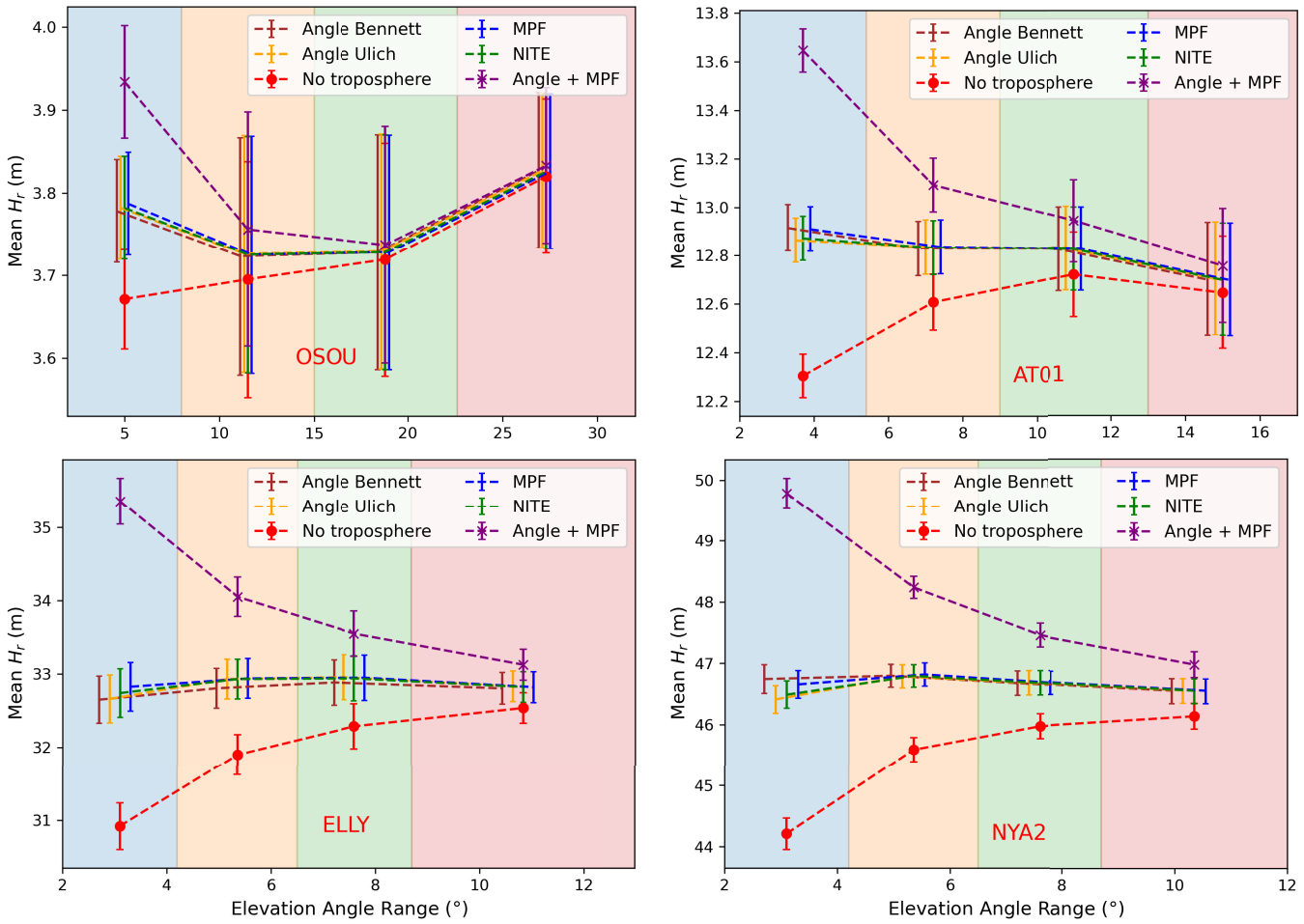

Fig. 9. 180-day mean H_r and 1σ errorbar from GNSS data at different elevation angle ranges (indicated by the colored background) for four sites from DOY 1–180, 2022. The error bars are shifted in the x-axis direction to avoid overlapping. Notice that each graph has different x- and y-axis ranges.

series. The tropospheric error is proportional to the reflector height, which makes this discrepancy obvious for stations with a large reflector height. In Fig. 8, it is evident that applying strategy-e (no troposphere) leads to a significant elevation-dependent error. H_r from low elevation angle data is negatively biased compared to the results from higher elevation angles, with discrepancies of up to 2 m for the NYA2 ($H_r \approx 48$ m). Furthermore, applying strategy-f (angle + MPF) creates an elevation-dependent bias with similar magnitudes but in the reversed direction. On the other hand, strategy-b (MPF delay), strategy-d (NITE formula), and the bending angle corrections (strategy-a and strategy-c) all seem to successfully remove the large part of the elevation angle dependence.

Fig. 9 provides a summary of the 180-day elevation range cutting experiment for all four sites. The average H_r retrieved from data within different elevation angle ranges, along with 1σ error, is plotted as a function of elevation angle range. To obtain the 1σ error, we fit a smooth B-spline trend to the H_r results and calculated the standard deviation of the detrended residuals series. Results from strategy-e (no troposphere) and strategy-f (angle + MPF) are symmetrically positioned below and above the other results. From Fig. 9, we can see that the bending angle correction and the MPF delay give corrections very close to each other. The "angle + MPF" is almost like applying the bending angle correction (or MPF delay) twice. The tropospheric error affects the H_r nonlinearly, which explains the magnitude difference observed in the symmetric pattern in Fig. 9.

For OSOU and AT01, some unusual elevation angle dependence is observed at high elevation angles (above 12°), where tropospheric errors are quite small. This could be attributed to other elevation-dependent factors, such as wave height [31] and antenna phase center [45]. Also, note that the NITE formula naturally incorporates Earth's curvature effect, while it is not corrected for other results presented in Fig. 9. Consequently, we are careful not to interpret results at the centimeter level here. In stations situated higher above sea level, like NYA2 and ELLY, the bias resulting from the "no troposphere" and "angle + MPF" can reach 1–3 m, well above the level of uncertainty of this experiment.

The elevation angle range cutting experiment confirmed that applying a combination of the bending angle correction [see (25)] and the path delay correction [see (26)] is overcompensating for GNSS-IR tropospheric error. Applying no tropospheric correction also introduces a large elevation-dependent error, as expected. The results align with the theory in Section II and simulation in Section III, where we showed

that the geometric displacement error is a lot smaller than the path delay.

With the elevation range cutting experiment, we cannot differentiate between the bending angle correction, the MPF delay approach, and the NITE formula, as their differences are smaller than the noise level (1σ) and the results are also impacted by other elevation angle dependent error sources [31], [45].

B. Comparison With Tide Gauge

We processed one year of GNSS data from four stations and compared the sea-level results with data from nearby tide gauges. To ensure stable H_r solutions and maximize the exposure to tropospheric errors for investigation, we set the elevation angle ranges as follows: 2°–6° for ELLY, 2.5°–6° for NYA2, 2°–8° for OSOU, and 2°–7° for SC02. Unfortunately, it is still difficult to compare absolute sea level from GNSS-IR and tide gauges. First, the use of different geodetic datums for GNSS and tide gauge data can introduce uncertainties. Second, we did not apply antenna phase center corrections for GNSS-IR as this option was not yet available. Instead, the sea level from the tide gauges was subtracted from the GNSS-IR H_r (reversed) results to create a zero-mean residual series. We compared different tropospheric correction strategies using only the random error evolution over time of the zero-mean residuals. We tested four of the previously used six strategies. The "no troposphere" and "angle + MPF" were not included.

Fig. 10 depicts one-year zero-mean residuals of GNSS-IR H_r for the ELLY station, using a nearby tide gauge as a reference. It is evident that the bending angle correction with the Bennett equation [see Fig. 10(a)] leads to a nonstationary residual series throughout this one-year period. The ELLY station is situated on the west coast of North America, where a higher amount of water vapor is present in the atmosphere during the summer season (middle of the year). This proves that by neglecting water vapor effects, the Bennett equation introduces a seasonal error. Similar findings are observed for NYA2 with $H_r \approx 48$ m. The summer–winter bias is about 10 cm for NYA2 and ELLY. For OSOU with $H_r \approx 3.7$ m, this effect is barely visible.

The winter–summer biases in the results with the Bennett equation [see Fig. 10(a)] become more evident when considering daily average residuals (yellow dots in Fig. 10). Visually, we can see that the daily average residuals from the NITE formula [see Fig. 10(d)] are less scattered than the MPF delay approach [see Fig. 10(b)] and the bending angle correction with Ulich equation [see Fig. 10(c)]. This observation is supported by the standard deviation of the daily average residuals. The standard deviation of the daily average residuals of the NITE formula [see Fig. 10(d)] is 0.045 m, while it is 0.056 m for the Ulich bending angle correction [see Fig. 10(c)] and 0.062 m for the MPF delay approach [see Fig. 10(b)] even though the original residual series (≈200 values per day) have a similar level of standard deviation (0.211 m for the MPF delay, 0.210 m for the Ulich bending angle correction, and 0.207 m for the NITE formula).

We used the Allan deviation to further quantify the random error pattern of the residual series. The Allan deviation,

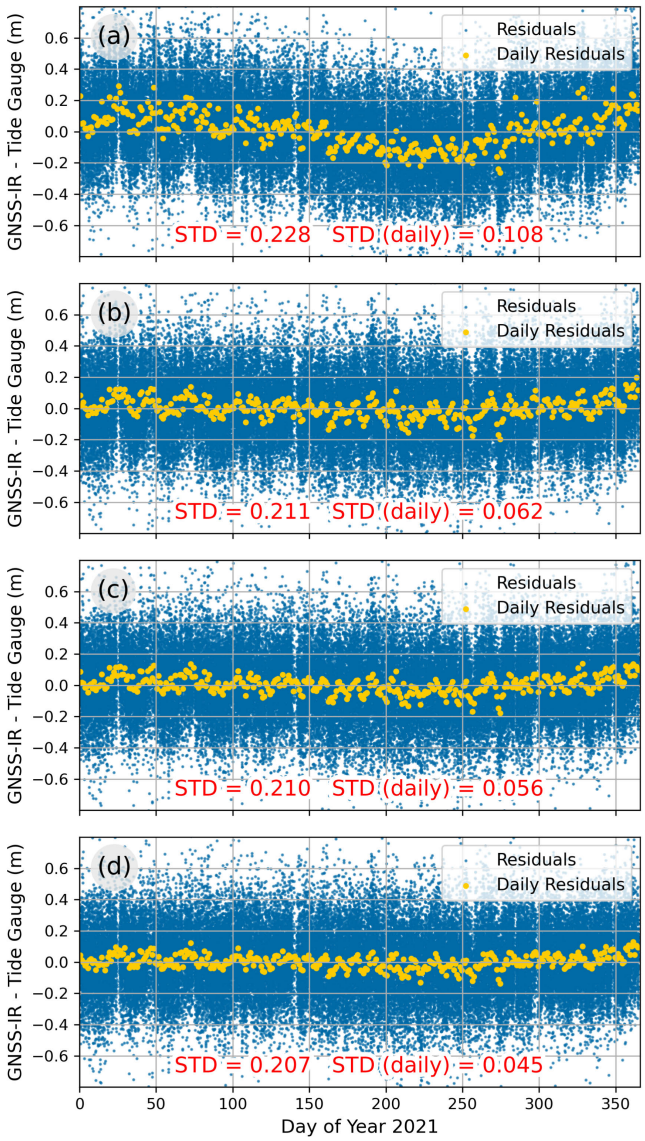

Fig. 10. Residuals and daily average residuals at ELLY of GNSS-IR H_r retrievals using tide gauge as reference: (a) angle Bennett, (b) MPF, (c) angle Ulich, and (d) NITE.

denoted as σ_{ADEV}, is defined with the equation

$$\sigma^2_{\mathrm{ADEV}}(\tau) = \frac{1}{2(M-1)} \sum_{i=1}^{M-1} [\overline{y_{i+1}} - \overline{y_i}]^2 \tag{27}$$

where $\overline{y_i}$ represents the ith fractional residual values averaged over the measurement interval, τ. The Allan deviation is widely used to study signal stability over different time scales. The challenges of applying the Allan deviation to the GNSS-IR sea-level residuals are the data gaps and nonuniform sampling time. For the four stations used, we have minimal data gaps. The residual series were linearly interpolated to generate uniform time series. For ELLY, with data from 2°–6°, we obtained ≈200 H_r retrievals per day (1 every 7.5 min but unevenly sampled), and each SNR series consisted of ≈15 min of observations. Therefore, we used 10 min as the interpolation step.

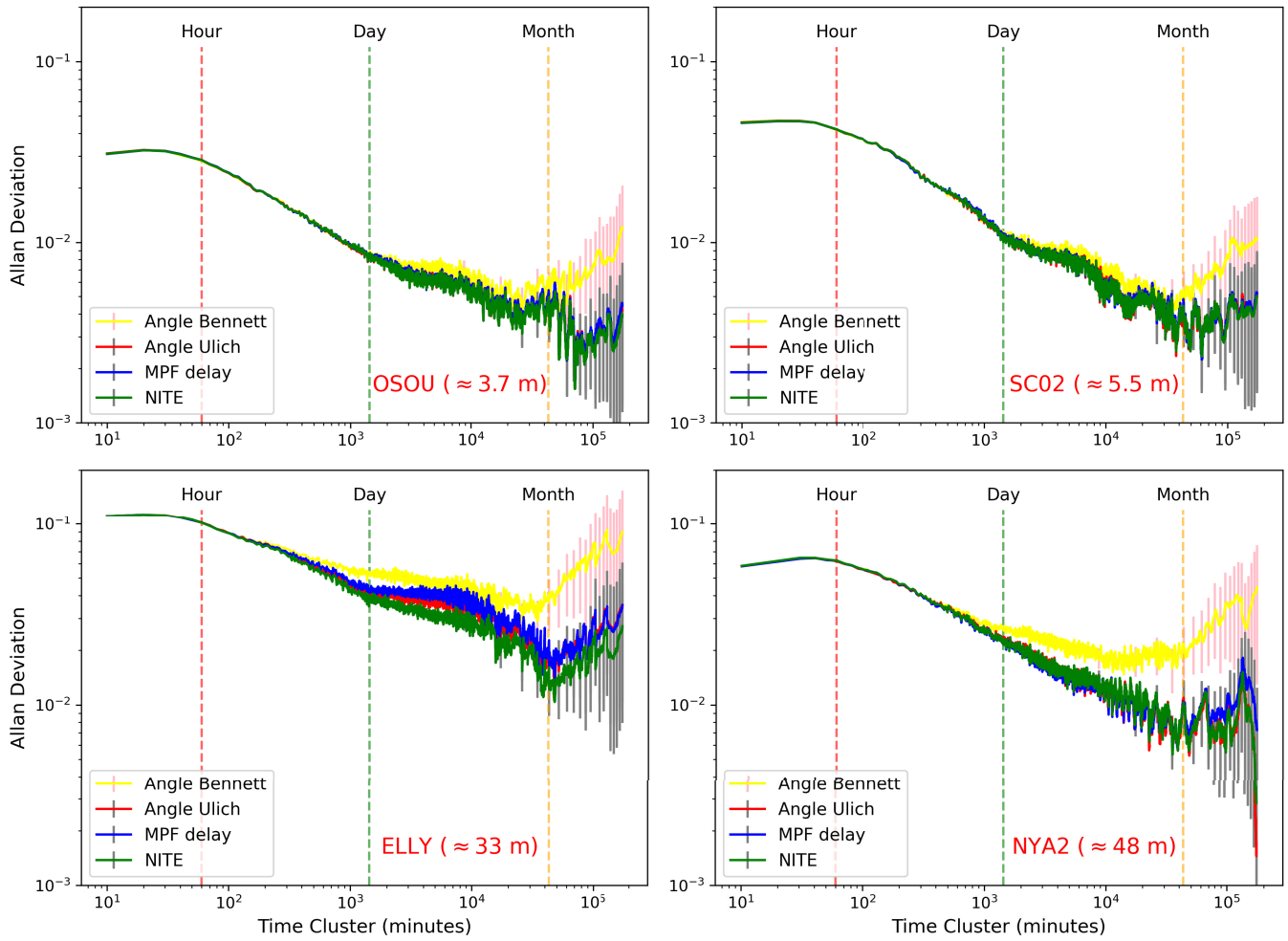

Fig. 11. Allan deviation of one-year water level residuals for four GNSS-IR stations with different reflector heights.

The Allan deviation σ–τ diagram for the four stations is presented in Fig. 11. Due to the fact that the residual series were interpolated to 10-min temporal resolution and the tide gauge data were also with similar temporal resolution (1 min for OSOU, 6 min for SC02/ELLY, and 10 min for NYA2), σ_{ADEV} for $\tau < 1$ h may contain errors. In addition, since we only used one year of data, σ_{ADEV} with $\tau > 2$ months is considered unreliable. From the figure, we can see that the Allan deviation of all four strategies remains the same for $\tau <$ 4 h. The long-term trend introduced by the Bennett equation becomes evident for all four stations. Specifically, the results from the Bennett bending angle correction (plotted yellow in Fig. 11) exhibit a larger σ_{ADEV} for the time scale from a few hours to a few months, which corresponds to the variation of water vapor.

Better long-term ($\tau > 4$ h) stability from the NITE formula is observed at the ELLY station but not at the other three stations. This is reasonable for the OSOU and SC02 stations with $H_r < 10$ m, where the reflection point is close to the antenna. NYA2 has a larger reflector height than ELLY, but the difference between the NITE formula, the MPF delay, and the bending angle correction (with the Ulich equation) is not noticeable. Comparing NYA2 and ELLY in Fig. 11, NYA2 also has a smaller σ_{ADEV}. This could potentially be attributed to differences in local atmospheric conditions, as NYA2 lies in the Arctic region (latitude ≈78.9°), while ELLY is located on an oil platform at North America's west coast.

From this experiment, we conclude that the bending angle correction with the Bennett equation should not be used in GNSS-IR analysis, as it introduces long-term (from a few hours to half a year) errors in the sea-level retrievals. The NITE formula appears to outperform the other approaches in some cases, but more experiments with large reflector heights are needed to draw a firm conclusion.

V. Discussion

With raytracing simulation and experimental data, we showed that numerically the bending angle correction and the MPF delay correction both give very similar results to the more rigorous NITE formula. For the MPF delay, such similarity is expected because the path delay [see (22)] is the dominating part of the NITE formula. From a physical perspective, the MPF delay approach can be interpreted as the "interferometric tropospheric path delay by neglecting Earth's curvature and the small-angle mapping function difference."

In the following, we address the bending angle correction. It solely relies on the atmospheric bending angle, which is highly correlated with the ground refractivity and the mapping function [62], [63], [64]. In a series of works, Yan and Ping [62] and [63] demonstrated that the atmospheric bending angle can be modeled as $\Delta e = 10^{-6} N_0 \,\mathrm{mpf} \cos e_T$, with mpf being the commonly used mapping function. With the help of this relationship [third line in (28)], we can reformulate the bending angle correction by (25) as

$$\begin{aligned}\tau_i &= 2H_r \sin e_A \\ &= 2H_r(\sin e_T \cos \Delta e + \sin \Delta e \cos e_T) \\ &\approx 2H_r \sin e_T + 2H_r \Delta e \cos e_T \\ &= 2H_r \sin e_T + 2 \cdot 10^{-6} H_r N_0 \overline{\mathrm{mpf}} \cos e_T \end{aligned} \tag{28}$$

where $\overline{\mathrm{mpf}}$ represents the averaged mapping function that is implicitly included in the Ulich/Bennett bending angle equation. At low elevation angles $\cos e_T \approx 1$, the bending angle correction is reformulated to an MPF delay [see (26)]. It is important to highlight that the bending angle correction poses theoretical issues. In the zenith direction, $\cos e_T = 0$, and the bending angle correction is 0, which violates the facts.

Phase-based GNSS-IR sea-level altimetry can make use of data that are very close to zenith [65], [66]. In the raytracing results (low-right part in Fig. 4), discrepancies between the bending angle correction and the NITE formula are evident in the range of 40°–90°. SNR-based GNSS-IR usually uses low-elevation-angle data. However, with some special setup, such as a cellphone [67] or horizontal-facing antennas [68], data from higher elevation angles (up to 60°) have also been used.

Equation (28) demonstrates that the bending angle correction is an approximation to the MPF delay at low elevation angles. However, it is necessary to adopt a better equation to calculate the atmospheric bending angle, such as the Ulich equation [40]. In Fig. 12, we plotted the bending angle equation error of the Bennett and Ulich equations (model value minus raytracing) w.r.t. the zenith wet delay (ZWD) for 14 radiosonde stations. The Ulich equation performs better and is more consistent in different ZWD situations. The experimental results presented in Section IV-B showed the time-varying error introduced by the Bennett equation. The water vapor content is also location-dependent; thus, the Bennett equation will also introduce different errors in different places.

The bending angle correction (with the Ulich equation), though not theoretically strict, is very convenient to apply for SNR-based GNSS-IR applications. The MPF delay approach is more complicated to implement than the bending angle correction and delivers similar performance at low elevation angles. However, at higher elevation angles, it performs better. The NITE formula proposed in this work is more complicated than both the MPF delay and the bending angle correction, but it is more rigorous.

Due to the refraction of the atmosphere: 1) the position of the reflection point is changed; 2) the GNSS signal propagates along a curved path; and 3) the signal speed is slower; 1) is parameterized by the atmospheric bending angle and addressed by the NITE geometric displacement error, together with Earth's curvature effects; and 2) and 3) are addressed in the NITE formula as the interferometric path delay. Both 1) and 2) are results of the "signal bending," while only 2), what we call the curve path effect, is considered in GNSS positioning and referred to as the bending effect [44]. This curve path (bending) effect is included in the mapping function; therefore, the MPF delay and the bending angle correction are both quantifying 2) and 3), with different levels of approximation. Furthermore, both the bending angle correction and the MPF delay approach assume a flat reflector surface, so the geometric displacement error is not applicable.

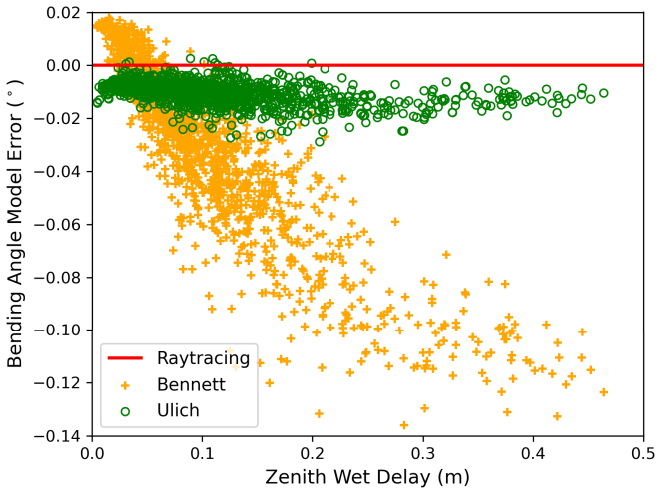

Fig. 12. Bending angle equation errors over ZWD at $e_T = 2°$ for 14 globally distributed radiosonde stations.

Data from higher elevation angles are less affected by the tropospheric error. However, the utilization of high-elevation data for GNSS-IR is discouraged by many other factors, including antenna gain patterns, physical obstructions in the local environment, and ocean roughness [31], [69]. Antennas positioned closer to the sea surface encounter less impact from tropospheric errors. Conversely, an antenna placed at a higher elevation captures more interferometric cycles, thereby enhancing temporal resolution. In places with large tidal changes [70], it becomes infeasible to maintain a GNSS antenna in close proximity to the sea surface continuously. The NITE tropospheric error formula, described in this study, performs better in such challenging situations. As a result, the applicability of GNSS-IR for sea-level monitoring is expanded.

VI. Conclusion

We deduced the NITE formula to calculate tropospheric corrections for ground-based GNSS-IR on a spherical Earth. This formula comprises two components: a geometric displacement error [see (11)] and a path delay [see (22)]. The geometric displacement error is based on specular reflection with a curved signal path and curved Earth surface. The path delay is obtained following the definition of the mapping function.

We validated the NITE formula using raytracing with radiosonde profiles, together with two previously proposed approaches: the bending angle correction and the MPF delay.

We found that, numerically, the geometric displacement error of the NITE formula is a lot smaller than the path delay. For a 20-m antenna, the geometric displacement error is less than 5% of the path delay part at 2° and even smaller at higher elevation angles (see Figs. 2 and 4). The NITE formula outperforms previous approaches in both subcomponents and total tropospheric error. We found that the inaccuracy in mapping function products can introduce a systematic bias to the NITE formula total tropospheric error, and the random error is limited by the representativeness of the average layer refractivity (see Fig. 6).

We tested six strategies for correcting tropospheric errors with two sets of experiments. Three of them, "no troposphere," "angle + MPF delay," and the "bending angle correction with Bennett equation," are rejected using elevation dependence and time-domain trend criterion. The NITE formula seems to outperform other approaches in one station (see Fig. 11), but more experiments with large reflector heights will be needed to draw a conclusion. In addition, we discussed the link between the bending angle correction, the MPF delay, and the NITE formula. We showed that at low elevation angles, the bending angle correction can be reformulated to an MPF delay [see (28)]. The source code of the NITE formula is submitted to an open repository [71].

Several approximations are made in the derivation of the NITE formula based on the geometry of ground-based GNSS-IR. Regarding the troposphere, we only considered the vertical distribution of the refractivity, neglecting horizontal gradients [72]. The finite distance of satellites is taken into account but only by approximations. The NITE formula heavily relies on determining the reflection point, which is solved using the small-angle approximation. Another factor that is not considered is the impact of the geoid, which can influence the curvature radius of the sea surface. In addition, the orientation of the sea surface is also influenced by the geoid [73].

The phase-based GNSS-IR, though more complicated and less robust, can reach higher accuracy and temporal resolution. Experiments with phase-based GNSS-IR can be used to assess the NITE formula in a different way. One challenge that we encountered in the experiment was the lack of meteorology data at the GNSS stations. The significant influence of the tropospheric error uncovered in the experiment (see Fig. 9) suggests that it is feasible to estimate the average layer refractivity along with the reflector height.

APPENDIX
TWO-STEP 2-D RAYTRACING FOR GNSS-IR

To validate the interferometric tropospheric error formula, it is necessary to carry out raytracing for both the direct and reflected signals. Raytracing for direct GNSS signals has been extensively studied in space geodesy [74], [75]. In this work, we adapt a 2-D raytracing tool we developed and validated in a previous study [76] to perform raytracing for the reflected signal. The direct 2-D raytracing is similar to the method employed for generating the Vienna mapping function [77]. With a given refractivity profile, the direct raytracing algorithm starts with an initial apparent elevation angle and calculates the signal path layer by layer. Usually, assuming an infinite satellite distance was considered to introduce negligible error

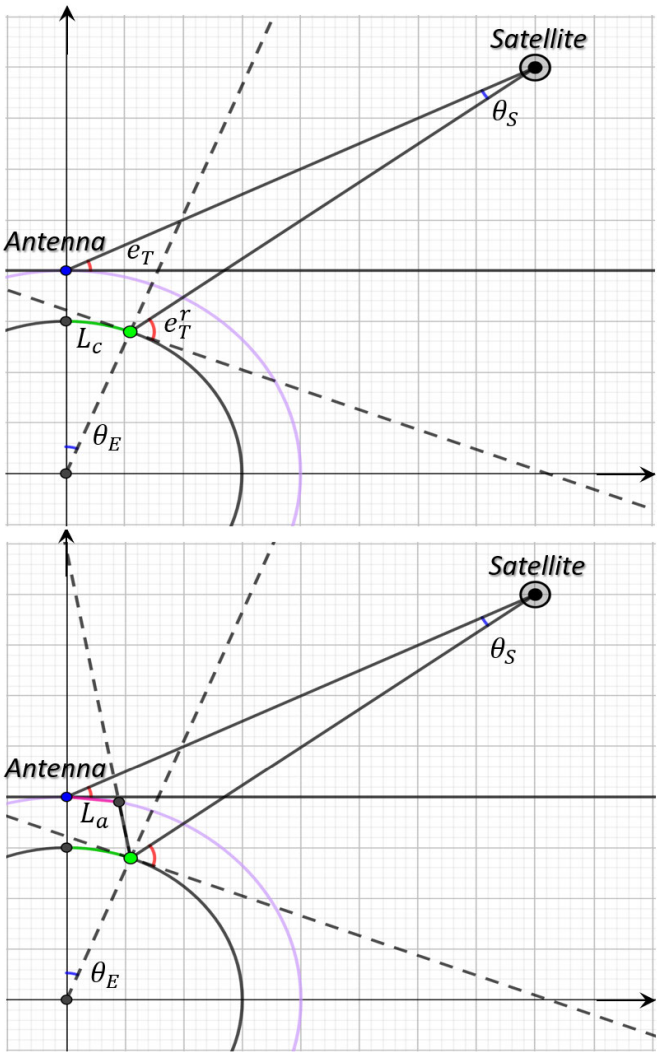

Fig. 13. Demonstration of steps 2 and 3 of the reflected signal raytracing.

in GNSS. Hence, the raytracing iteration terminates when the outgoing elevation angle at the top of the atmosphere is sufficiently close to the true elevation angle [77]. A major change that we have made is the use of the true elevation angle instead of the "out-going" elevation angle. The true elevation angle is calculated by extending a straight ray from the top of the atmosphere to the satellite orbit. Numerically, it only makes a minor difference, but it is theoretically more rigorous. Consequently, the geometric signal path for the direct and reflected signals can be accurately defined.

We simplified the raytracing for the reflected signal by using the specular reflection assumption. First, since we are considering a stratified atmosphere, the reflected signal is symmetric at two sides of the reflection point below the antenna. Second, we approximated the shape of the Earth as a sphere rather than an ellipsoid.

The procedures of raytracing are given as follows (see Fig. 13 for the variables used).

1) Direct signal raytracing is performed at the antenna with a given true elevation angle. This gives us the direct signal path. The satellite's coordinates in the Earth-centered 2-D Cartesian coordinate system are calculated using the true elevation angle and GNSS orbit radius.

2) L_c represents the arc length between the reflection point and the projection of the antenna on the big circle of the sea surface. With an initial L_c, the coordinate of the reflection point, Earth's center angle θ_E, and the satellite angle θ_S can be analytically calculated. The true elevation angle e_T^r for the reflected signal down-leg is obtained for this given L_c.
3) Raytracing the down-leg of the reflected signal using e_T^r and the refractivity profile down to the sea surface. By mirroring the down-leg signal over the perpendicular line at the reflection point, the up-leg path is obtained. The up-leg ray intersects with the Earth-centered circle that crosses the GNSS antenna, with an arc length L_a to the antenna. We compare this intersection point with the positioning of the GNSS antenna in this circle to determine if L_c is either too large or too small. Iterate until the up-leg ray intersects the circle with a distance <0.1 mm to the antenna. Since the reflector height is 100 m at maximum, the circle through the antenna and the sea surface are close to parallel locally. The iteration of L_c is done by subtracting L_a (can be negative) from L_c.
4) Calculate interferometric delay and tropospheric error by definition using the direct and reflected signal paths.

ACKNOWLEDGMENT

The geodetic research infrastructure at the Onsala site was supported by the Swedish Mapping, Cadastral and Land Registration Authority. The traditional tide gauge is operated in collaboration with the Swedish Meteorological and Hydrological Institute. The authors would like to express their gratitude to the global navigation satellite system (GNSS) reflection website (https://gnss-reflections.org/) for providing many useful tools.

DATA STATEMENT

The radiosonde data used in this study were obtained from the National Oceanic and Atmospheric Administration (NOAA) Integrated Global Radiosonde Archive (www.ncei.noaa.gov/products/weather-balloon/). The Vienna mapping function products and code were obtained from the VMF Data Server (https://vmf.geo.tuwien.ac.at/). High-rate global navigation satellite system (GNSS) data for SC02, AT01, and ELLY were downloaded from the Geodetic Facility for the Advancement of Geoscience (GAGE), together with the meteorology Receiver Independent Exchange Format (RINEX) files for ELLY. Meteorology data from AT01 and SC02 were obtained from Iowa State University Iowa Environmental Mesonet (https://mesonet.agron.iastate.edu/). GNSS data for NYA2 were available from the International GNSS Service (IGS) server hosted by Crustal Dynamics Data Information System (CDDIS). Meteorology data from NYA2 were obtained from the Geodetic Earth Observatory, Ny-Ålesund, Svalbard and Jan Mayen. Tide gauge data near ELLY and SC02 were obtained from NOAA's Center for Operational Oceanographic Products and Services (CO-OPS). Tide gauge data for NYA2 were obtained from "Se havnivå" of the Norwegian Mapping Authority. GNSS, meteorology, and tide gauge data at OSOU were collected by the Onsala Space Observatory and are available by contacting the corresponding author.

REFERENCES

[1] D. Dao, C. Rizos, and J. Wang, "Location-based services: Technical and business issues," *GPS Solutions*, vol. 6, no. 3, pp. 169–178, Dec. 2002.
[2] N. D. Pham, *The Economic Benefits of Commercial GPS Use in the U.S. and the Costs of Potential Disruption*. Belgrade, Serbia: NDP Consulting, 2011.
[3] J. Duan et al., "GPS meteorology: Direct estimation of the absolute value of precipitable water," *J. Appl. Meteorol.*, vol. 35, no. 6, pp. 830–838, Jun. 1996.
[4] S. Sokolovskiy, Y.-H. Kuo, C. Rocken, W. S. Schreiner, D. Hunt, and R. A. Anthes, "Monitoring the atmospheric boundary layer by GPS radio occultation signals recorded in the open-loop mode," *Geophys. Res. Lett.*, vol. 33, no. 12, pp. 12–15, Jun. 2006.
[5] K. M. Larson, E. E. Small, E. D. Gutmann, A. L. Bilich, J. J. Braun, and V. U. Zavorotny, "Use of GPS receivers as a soil moisture network for water cycle studies," *Geophys. Res. Lett.*, vol. 35, no. 24, Dec. 2008, Art. no. L24405.
[6] K. M. Larson, "Unanticipated uses of the global positioning system," *Annu. Rev. Earth Planet. Sci.*, vol. 47, no. 1, pp. 19–40, May 2019.
[7] K.-D. Park, R. S. Nerem, M. S. Schenewerk, and J. L. Davis, "Site-specific multipath characteristics of global IGS and CORS GPS sites," *J. Geodesy*, vol. 77, no. 12, pp. 799–803, Jun. 2004.
[8] Y. Georgiadou and A. Kleusberg, "On carrier signal multipath effects in relative GPS positioning," *Manuscripta geodaetica*, vol. 13, no. 3, pp. 172–179, 1988.
[9] K. M. Larson, R. D. Ray, F. G. Nievinski, and J. T. Freymueller, "The accidental tide gauge: A GPS reflection case study from Kachemak bay, Alaska," *IEEE Geosci. Remote Sens. Lett.*, vol. 10, no. 5, pp. 1200–1204, Sep. 2013.
[10] P. Milnarich and W. L. Shepherd, "Prediction of apparent elevation angle from specified position for an object in the troposphere," *J. Appl. Meteorol.*, vol. 5, no. 5, pp. 722–725, Oct. 1966.
[11] K. M. Larson, J. S. Löfgren, and R. Haas, "Coastal sea level measurements using a single geodetic GPS receiver," *Adv. Space Res.*, vol. 51, no. 8, pp. 1301–1310, Apr. 2013.
[12] J. S. Löfgren and R. Haas, "Sea level measurements using multi-frequency GPS and GLONASS observations," *EURASIP J. Adv. Signal Process.*, vol. 2014, no. 1, pp. 1–13, Dec. 2014.
[13] X. Wang, X. He, and Q. Zhang, "Evaluation and combination of quad-constellation multi-GNSS multipath reflectometry applied to sea level retrieval," *Remote Sens. Environ.*, vol. 231, Sep. 2019, Art. no. 111229.
[14] F. Geremia-Nievinski et al., "SNR-based GNSS reflectometry for coastal sea-level altimetry: Results from the first IAG inter-comparison campaign," *J. Geodesy*, vol. 94, no. 8, p. 70, Aug. 2020.
[15] J. Strandberg, "New methods and applications for interferometric GNSS reflectometry," Ph.D. dissertation, Dept. Space, Earth Environ., Chalmers Univ. Technol., Gothenburg, Sweden, 2020.
[16] A. Santamaría-Gómez and C. Watson, "Remote leveling of tide gauges using GNSS reflectometry: Case study at spring bay, Australia," *GPS Solutions*, vol. 21, no. 2, pp. 451–459, Apr. 2017.
[17] G. G. Bennett, "The calculation of astronomical refraction in marine navigation," *J. Navigat.*, vol. 35, no. 2, pp. 255–259, May 1982.
[18] C. Roesler and K. M. Larson, "Software tools for GNSS interferometric reflectometry (GNSS-IR)," *GPS Solutions*, vol. 22, no. 3, pp. 1–10, Jul. 2018.
[19] S. D. P. Williams and F. G. Nievinski, "Tropospheric delays in ground-based GNSS multipath reflectometry—Experimental evidence from coastal sites," *J. Geophys. Res., Solid Earth*, vol. 122, no. 3, pp. 2310–2327, Mar. 2017.
[20] T. Nikolaidou, M. C. Santos, S. D. P. Williams, and F. Geremia-Nievinski, "Raytracing atmospheric delays in ground-based GNSS reflectometry," *J. Geodesy*, vol. 94, no. 8, pp. 1–12, Aug. 2020.
[21] R. N. Treuhaft, S. T. Lowe, C. Zuffada, and Y. Chao, "2-cm GPS altimetry over Crater Lake," *Geophys. Res. Lett.*, vol. 28, no. 23, pp. 4343–4346, Dec. 2001.
[22] F. Fabra et al., "Phase altimetry with dual polarization GNSS-R over sea ice," *IEEE Trans. Geosci. Remote Sens.*, vol. 50, no. 6, pp. 2112–2121, Jun. 2012.
[23] T. Nikolaidou, M. C. Santos, S. D. P. Williams, and F. Geremia-Nievinski, "Development and validation of comprehensive closed formulas for atmospheric delay and altimetry correction in ground-based GNSS-R," *IEEE Trans. Geosci. Remote Sens.*, vol. 61, 2023, Art. no. 5801007.

[24] D. Peng, E. M. Hill, L. Li, A. D. Switzer, and K. M. Larson, "Application of GNSS interferometric reflectometry for detecting storm surges," *GPS Solutions*, vol. 23, no. 2, pp. 1–11, Apr. 2019.

[25] M. Ye, S. Jin, and Y. Jia, "Ten-minute sea-level variations from combined multi-GNSS multipath reflectometry based on a weighted iterative least-square method," *IEEE Trans. Geosci. Remote Sens.*, vol. 60, 2022, Art. no. 4208510.

[26] S. Xie, "Continuous measurement of sea ice freeboard with tide gauges and GNSS interferometric reflectometry," *Remote Sens. Environ.*, vol. 280, Oct. 2022, Art. no. 113165.

[27] N. Wang et al., "Sea-level monitoring and ocean tide analysis based on multipath reflectometry using received strength indicator data from multi-GNSS signals," *IEEE Trans. Geosci. Remote Sens.*, vol. 60, 2022, Art. no. 4211513.

[28] N. Roussel et al., "Sea level monitoring and sea state estimate using a single geodetic receiver," *Remote Sens. Environ.*, vol. 171, pp. 261–277, Dec. 2015.

[29] S. Tabibi, F. Geremia-Nievinski, O. Francis, and T. van Dam, "Tidal analysis of GNSS reflectometry applied for coastal sea level sensing in Antarctica and Greenland," *Remote Sens. Environ.*, vol. 248, Jul. 2020, Art. no. 111959.

[30] X. Wang, X. He, R. Xiao, M. Song, and D. Jia, "Millimeter to centimeter scale precision water-level monitoring using GNSS reflectometry: Application to the South-to-North Water Diversion Project, China," *Remote Sens. Environ.*, vol. 265, Nov. 2021, Art. no. 112645.

[31] X. Wang, X. He, J. Shi, S. Chen, and Z. Niu, "Estimating sea level, wind direction, significant wave height, and wave peak period using a geodetic GNSS receiver," *Remote Sens. Environ.*, vol. 279, Sep. 2022, Art. no. 113135.

[32] T. Gravalon, L. Seoane, G. Ramillien, J. Darrozes, and L. Roblou, "Determination of weather-induced short-term sea level variations by GNSS reflectometry," *Remote Sens. Environ.*, vol. 279, Sep. 2022, Art. no. 113090.

[33] E. L. Fleming, S. Chandra, J. J. Barnett, and M. Corney, "Zonal mean temperature, pressure, zonal wind and geopotential height as functions of latitude," *Adv. Space Res.*, vol. 10, no. 12, pp. 11–59, Jan. 1990.

[34] J. Saastamoinen, "Contributions to the theory of atmospheric refraction—Part II. Refraction corrections in satellite geodesy," *Bull. Géodésique*, vol. 47, no. 1, p. 428, 1973.

[35] R. C. Stone, "An accurate method for computing atmospheric refraction," *Publications Astronomical Soc. Pacific*, vol. 108, p. 1051, Nov. 1996.

[36] A. E. Niell, "Global mapping functions for the atmosphere delay at radio wavelengths," *J. Geophys. Res., Solid Earth*, vol. 101, no. B2, pp. 3227–3246, Feb. 1996.

[37] D. Landskron and J. Böhm, "VMF3/GPT3: Refined discrete and empirical troposphere mapping functions," *J. Geodesy*, vol. 92, no. 4, pp. 349–360, Apr. 2018.

[38] M. Bevis, S. Businger, T. A. Herring, C. Rocken, R. A. Anthes, and R. H. Ware, "GPS meteorology: Remote sensing of atmospheric water vapor using the global positioning system," *J. Geophys. Res., Atmos.*, vol. 97, no. D14, pp. 15787–15801, Oct. 1992.

[39] G. Elgered, J. M. Johansson, B. O. Rönnäng, and J. L. Davis, "Measuring regional atmospheric water vapor using the Swedish permanent GPS network," *Geophys. Res. Lett.*, vol. 24, no. 21, pp. 2663–2666, Nov. 1997.

[40] B. L. Ulich, "Millimeter wave radio telescopes: Gain and pointing characteristics," *Int. J. Infr. Millim. Waves*, vol. 2, no. 2, pp. 293–310, Mar. 1981.

[41] J. M. Rüeger, "Refractive index formulae for radio waves," in *Proc. FIG Tech. Program*, Washington, DC, USA, 2002, pp. 1–13.

[42] S. Kwok, "A spherical Earth," in *Our Place Universe*. Cham, Switzerland: Springer, 2017, pp. 33–48.

[43] F. Zus, G. Dick, J. Dousa, and J. Wickert, "Systematic errors of mapping functions which are based on the VMF1 concept," *GPS Solutions*, vol. 19, no. 2, pp. 277–286, Apr. 2015.

[44] G. Möller and D. Landskron, "Atmospheric bending effects in GNSS tomography," *Atmos. Meas. Techn.*, vol. 12, no. 1, pp. 23–34, Jan. 2019.

[45] R. Dach, L. Simon, W. Peter, and F. Pierre, *Bernese GNSS Software Version 5.2*. Bern, Switzerland: Univ. Bern, Nov. 2015.

[46] T. Hobiger and N. Jakowski, "Atmospheric signal propagation," in *Springer Handbook of Global Navigation Satellite Systems*, vol. 6, no. 1. Cham, Switzerland: Springer, 2017, pp. 165–193.

[47] K. Lagler, M. Schindelegger, J. Böhm, H. Krásná, and T. Nilsson, "GPT2: Empirical slant delay model for radio space geodetic techniques," *Geophys. Res. Lett.*, vol. 40, no. 6, pp. 1069–1073, Mar. 2013.

[48] T. A. Herring, R. W. King, M. A. Floyd, and S. C. McClusky, *GAMIT Reference Manual: GPS Analysis at MIT, Release 10.6*. Cambridge, MA, USA: Massachusetts Institute of Technology, Jun. 2010.

[49] H. Yan, G. Zhang, P. Guo, and Z. Hong, "Discussion and comparison of the mapping functions in radio frequencies," *Terr., Atmos. Ocean. Sci.*, vol. 13, no. 4, p. 563, 2002.

[50] D. Landskron, "Modeling tropospheric delays for space geodetic techniques," Ph.D. dissertation, Dept. Geodesy Geoinf., Vienna Univ. Technol., Vienna, Austria, 2017.

[51] *VMF Data Server*. Accessed: Aug. 16, 2022. [Online]. Available: https://vmf.geo.tuwien.ac.at/

[52] W. Zhang et al., "The use of ground-based GPS precipitable water measurements over China to assess radiosonde and ERA-interim moisture trends and errors from 1999 to 2015," *J. Climate*, vol. 30, no. 19, pp. 7643–7667, Oct. 2017.

[53] A. M. Semmling et al., "On the retrieval of the specular reflection in GNSS carrier observations for ocean altimetry," *Radio Sci.*, vol. 47, no. 6, pp. 1–13, Dec. 2012.

[54] I. Durre, R. S. Vose, and D. B. Wuertz, "Overview of the integrated global radiosonde archive," *J. Climate*, vol. 19, no. 1, pp. 53–68, Jan. 2006.

[55] R. Minzner et al., "Defining constants, equations, and abbreviated tables of the 1975 U.S. Standard Atmosphere," NASA, Washington, DC, USA, Tech. Rep. R-459, May 1976.

[56] F. Geremia-Nievinski, M. Makrakis, and S. Tabibi. (Feb. 2020). *Inventory of Published GNSS-R Stations, with Focus on Ocean as Target and SNR as Observable*. [Online]. Available: https://zenodo.org/record/3668360

[57] J. Boehm, B. Werl, and H. Schuh, "Troposphere mapping functions for GPS and very long baseline interferometry from European Centre for Medium-Range Weather Forecasts operational analysis data," *J. Geophys. Res., Solid Earth*, vol. 111, no. B2, pp. 1–9, Feb. 2006.

[58] J. L. Davis, G. Elgered, A. E. Niell, and C. E. Kuehn, "Ground-based measurement of gradients in the 'wet' radio refractivity of air," *Radio Sci.*, vol. 28, no. 6, pp. 1003–1018, 1993.

[59] K. M. Larson. (Oct. 2021). *kristinemlarson/gnssrefl: First Release*. [Online]. Available: https://zenodo.org/record/5601495

[60] JPL. *PPPX*. Accessed: Nov. 23, 2022. [Online]. Available: https://pppx.gdgps.net/

[61] J. Ping, H. Yan, G. Wang, Z. Qian, R. Zhou, and F. Shu, "A comparison of different tropospheric mapping functions by elevation cut-off tests," *Monthly Notices Roy. Astronomical Soc.*, vol. 287, no. 4, pp. 812–816, Jun. 1997.

[62] H. Yan and J. Ping, "The generator function method of the tropospheric refraction corrections," *Astronomical J.*, vol. 110, p. 934, Aug. 1995.

[63] H. Yan, "New continued fraction form of the mapping functions of atmospheric refraction corrections," *Astronomical Astrophysical Trans.*, vol. 16, no. 1, pp. 61–73, May 1998.

[64] P. Feng, R. Haas, G. Elgered, and J. Strandberg, "Calibrating tropospheric errors on ground-based GNSS reflectometry: Calculation of bending and delay effects," in *Proc. 24th EGU General Assembly*, Mar. 2022, Paper no. EGU22-12698.

[65] J. S. Löfgren, R. Haas, H.-G. Scherneck, and M. S. Bos, "Three months of local sea level derived from reflected GNSS signals," *Radio Sci.*, vol. 46, no. 6, pp. 1–12, Dec. 2011.

[66] Y. He, F. Gao, T. Xu, X. Meng, and N. Wang, "Coastal altimetry using interferometric phase from GEO satellite in quasi-zenith satellite system," *IEEE Geosci. Remote Sens. Lett.*, vol. 19, pp. 1–5, 2022.

[67] Z. Liu, L. Du, P. Zhou, Z. Liu, Z. Zhang, and Z. Xu, "Performance assessment of GNSS-IR altimetry using signal-to-noise ratio data from a Huawei P30 smartphone," *GPS Solutions*, vol. 26, no. 2, pp. 1–10, Apr. 2022.

[68] D. J. Purnell, N. Gomez, W. Minarik, D. Porter, and G. Langston, "Precise water level measurements using low-cost GNSS antenna arrays," *Earth Surf. Dyn.*, vol. 9, no. 3, pp. 673–685, Jun. 2021.

[69] D. Purnell, N. Gomez, N. H. Chan, J. Strandberg, D. M. Holland, and T. Hobiger, "Quantifying the uncertainty in ground-based GNSS-reflectometry sea level measurements," *IEEE J. Sel. Topics Appl. Earth Observ. Remote Sens.*, vol. 13, pp. 4419–4428, 2020.

[70] C. Garrett, "Tidal resonance in the bay of Fundy and Gulf of Maine," *Nature*, vol. 238, no. 5365, pp. 441–443, Aug. 1972. [Online]. Available: https://www.nature.com/articles/238441a0

[71] P. Feng. (Jun. 2023). *Implementation of the NITE Model for Ground-Based GNSS-IR Tropospheric Correction*. [Online]. Available: https://zenodo.org/record/8082671

[72] G. Elgered, T. Ning, P. Forkman, and R. Haas, "On the information content in linear horizontal delay gradients estimated from space geodesy observations," *Atmos. Meas. Techn.*, vol. 12, no. 7, pp. 3805–3823, Jul. 2019.

[73] C. Hirt, U. Marti, B. Bürki, and W. E. Featherstone, "Assessment of EGM2008 in Europe using accurate astrogeodetic vertical deflections and omission error estimates from SRTM/DTM2006.0 residual terrain model data," *J. Geophys. Res., Solid Earth*, vol. 115, no. B10, p. 10404, Oct. 2010.

[74] T. Hobiger, R. Ichikawa, T. Takasu, Y. Koyama, and T. Kondo, "Ray-traced troposphere slant delays for precise point positioning," *Earth, Planets Space*, vol. 60, no. 5, pp. e1–e4, May 2008.

[75] V. Nafisi et al., "Comparison of ray-tracing packages for troposphere delays," *IEEE Trans. Geosci. Remote Sens.*, vol. 50, no. 2, pp. 469–481, Feb. 2012.

[76] P. Feng, F. Li, J. Yan, F. Zhang, and J.-P. Barriot, "Assessment of the accuracy of the saastamoinen model and VMF1/VMF3 mapping functions with respect to ray-tracing from radiosonde data in the framework of GNSS meteorology," *Remote Sens.*, vol. 12, no. 20, p. 3337, Oct. 2020.

[77] J. Boehm and H. Schuh, "Vienna mapping functions," in *Proc. 16th Work. Meeting Eur. VLBI Eodesy Astrometry*, Leipzig, Germany, May 2003, pp. 131–143.

Peng Feng (Member, IEEE) received the Ph.D. degree in geodesy and geophysics from Wuhan University, Wuhan, China, and the University of French Polynesia, Puna'auia, French Polynesia, in 2021.

He is currently a Post-Doctoral Researcher with the Onsala Space Observatory, Onsala, Sweden, supported by a grant from the Hasselblad Foundation. His research interests include atmospheric effects on space geodesy and environmental remote sensing with different space geodetic techniques.

Rüdiger Haas is currently a Full Professor of space geodesy with the Department of Space, Earth and Environment, Chalmers University of Technology, Gothenburg, Sweden. He is the Head of the Research Group for Space Geodesy and Geodynamics and is responsible for the geoscience activities at the Onsala Space Observatory, Onsala, Sweden. His research is focused on space geodetic techniques, such as global navigation satellite systems, including global navigation satellite system (GNSS) reflectometry and very long baseline interferometry (VLBI).

Gunnar Elgered received the Ph.D. degree from the Chalmers University of Technology, Gothenburg, Sweden, in 1983.

Since 2023, he has been a Professor Emeritus of electrical measurements with the Department of Space, Earth and Environment, Chalmers University of Technology. His research is focused on remote sensing of the atmosphere using space geodetic techniques and microwave radiometry.